remote sensing

MDPI

Article

Using Voting-Based Ensemble Classifiers to Map Invasive *Phragmites australis*

Connor J. Anderson *, Daniel Heins, Keith C. Pelletier and Joseph F. Knight

Department of Forest Resources, University of Minnesota, 1530 Cleveland Ave. N, St. Paul, MN 55108, USA; dheins@umn.edu (D.H.); pelle155@umn.edu (K.C.P.); jknight@umn.edu (J.F.K.)
* Correspondence: and03010@umn.edu

Abstract: Machine learning is frequently combined with imagery acquired from uncrewed aircraft systems (UASs) to detect invasive plants. Having prior knowledge of which machine learning algorithm will produce the most accurate results is difficult. This study examines the efficacy of a voting-based ensemble classifier to identify invasive *Phragmites australis* from three-band (red, green, blue; RGB) and five-band (red, green, blue, red edge, near-infrared; multispectral; MS) UAS imagery acquired over multiple Minnesota wetlands. A Random Forest, histogram-based gradient-boosting classification tree, and two artificial neural networks were used within the voting-based ensemble classifier. Classifications from the RGB and multispectral imagery were compared across validation sites both with and without post-processing from an object-based image analysis (OBIA) workflow (post-machine learning OBIA rule set; post-ML OBIA rule set). Results from this study suggest that a voting-based ensemble classifier can accurately identify invasive *Phragmites australis* from RGB and multispectral imagery. Accuracies greater than 80% were attained by the voting-based ensemble classifier for both the RGB and multispectral imagery. The highest accuracy, 91%, was achieved when using the multispectral imagery, a canopy height model, and a post-ML OBIA rule set. The study emphasizes the need for further research regarding the accurate identification of *Phragmites australis* at low stem densities.

Keywords: *Phragmites australis*; UAS; machine learning; voting-based ensemble classifier; invasive species; multispectral

check for updates

Citation: Anderson, C.J.; Heins, D.; Pelletier, K.C.; Knight, J.F. Using Voting-Based Ensemble Classifiers to Map Invasive *Phragmites australis*. *Remote Sens.* **2023**, *15*, 3511. https://doi.org/10.3390/rs15143511

Academic Editors: No-Wook Park, Kiwon Lee and Kwangseob Kim

Received: 15 May 2023
Revised: 10 July 2023
Accepted: 11 July 2023
Published: 12 July 2023

Copyright: © 2023 by the authors. Licensee MDPI, Basel, Switzerland. This article is an open access article distributed under the terms and conditions of the Creative Commons Attribution (CC BY) license (https://creativecommons.org/licenses/by/4.0/).

1. Introduction

Wetlands are an important natural resource that provide multiple economic, environmental, and cultural services. They sequester carbon [1], filter water [2], and provide food for humans and fauna [2]. These ecosystems are currently facing numerous threats, such as removal through land conversion and biological invasions. Estimates of global wetland loss range from 33% to 57% [3,4], and roughly 53% of the wetlands in the conterminous United States have been lost between 1780–1980 [5]. Wetland loss in the Upper Midwest during the same 200-year period was estimated to be 35% in South Dakota, 42% in Minnesota, 46% in Wisconsin, 49% in North Dakota, 50% in Michigan, and 89% in Iowa [5]. Biological invasions have been particularly devastating to wetland flora and fauna diversity. Invasive wetland plants, in particular, have been documented to change nutrient and water cycles [6–8], decrease water quality [6], and reduce the diversity of native species [9,10]. The negative effects of invasive wetland plants result in direct impacts on people through reduced wetland benefits and monetary loss. It is estimated that the cost associated with invasive aquatic species within the United States is around USD 110 million annually [11]. Efficient control and removal of invasive wetland plants depends on knowing the geographic location of infestations. However, obtaining the geographic locations of invasive plant populations can be challenging due to the cryptic nature of their invasion [12,13].

Minnesota has categorized *Phragmites australis* (Cav.) Trin. Ex Steud. ssp. *australis* (hereafter *Phragmites*), an invasive wetland grass, is a prohibited control species [14]. This designation forbids the sale, transportation, and importation of the plant. Detected populations of prohibited control species within Minnesota are also legally required to be removed. *Phragmites* grows in dense, monotypic stands, and it can reach a height of 5 m. It can spread through a combination of aerial seed dispersal and rhizomes. This plant has expanded its range to each of the 48 conterminous United States since its initial introduction to the United States in either the 18th or 19th century [15]. The rapid spread of *Phragmites* has been possible due to its salinity tolerance [16], the ability to capitalize on human-caused habitat change [17], and its fast growth rate [18]. Spread within Minnesota has been further facilitated by the use of the plant in wastewater treatment facilities. Invasive *Phragmites* has caused harm to Minnesota wetlands by changing wetland hydrology, altering nutrient cycles [19–22], and causing a reduction of biodiversity [23,24]. A native *Phragmites* genotype (*Phragmites australis* Trin. Ex. Steud. ssp. *americanus* Saltonst., P.M. Peterson and Soreng) is also present within Minnesota. However, the native *Phragmites* genotype is not as aggressive as the invasive *Phragmites*, and it generally grows in mixed stands of native herbaceous wetland vegetation. To date, extensive in situ mapping of *Phragmites* has been completed within Minnesota. Populations have been reported to the Early Detection and Distribution Mapping System (EDDMapS) [25], which is an online invasive species database. A total of 1537 populations of invasive *Phragmites* has been cataloged in Minnesota using EDDMapS as of March 2023 [25] (accessed on 23 March 2023).

Despite the scale at which *Phragmites* has been mapped within Minnesota, physical mapping methods suffer from limitations. Accessibility to target survey areas may be limited physically, such as the inability to access flooded or remote wetlands or access private land. Further challenges are faced at larger geographic scales due to the changing inter- and intra-annual distributions of *Phragmites*. For example, the distribution of *Phragmites* may change before the completion of a statewide Minnesota survey strictly using in situ methods. Remote sensing presents a possible solution to overcome physical mapping limitations for the detection and monitoring of *Phragmites*. Detection and monitoring of *Phragmites* at large geographic scales has been investigated using satellite imagery [26–30]. Laba et al. (2008) [28] classified multiple vegetation types within the Hudson River National Estuarine Research Reserve using Quickbird imagery. They achieved a user's accuracy of 76% and a producer's accuracy of 100% for the *Phragmites* class. Bourgeau-Chavez et al. (2013) [29] mapped *Phragmites* across the Great Lakes Basin with 87% accuracy when using PALSAR imagery. A limitation when using satellite imagery for mapping *Phragmites* is the larger minimum mapping unit. The use of higher resolution imagery is likely needed to accurately detect and monitor plant invasions, such as for *Phragmites* [31,32]. Uncrewed Aircraft Systems (UASs) are a suitable choice for *Phragmites* surveillance and monitoring. These platforms offer customizable data acquisition (e.g., timing, vehicle type, sensor type, image acquisition parameters, etc.) and provide very high-resolution imagery (pixel size smaller than 10 cm). UASs can provide resource managers the ability to quickly collect highly accurate data over tens to hundreds of hectares that can be used to survey for *Phragmites* and monitor treatment results.

Several researchers have investigated the application of UAS for mapping *Phragmites*. Husson et al. (2014) [33] examined whether *Phragmites* could be visually detected within UAS imagery in Sweden. They concluded that *Phragmites* could be reliably identified by visual image interpreters, and the use of automated classification methods should be explored. Samiappan et al. (2016) [34] used a texture-based strategy with a Support Vector Machine (SVM) to attain classification accuracies of 85% for *Phragmites*. Subsequent research by Samiappan et al. (2017) [35] achieved an overall accuracy of 91% when using five-band multispectral imagery (blue, green, red, red edge, and near-infrared) with an SVM classifier. Others have explored the use of additional classification methods. Abeysinghe et al. (2019) [36] tested different machine-learning classifiers and whether object-based classifications attained higher classification accuracies than pixel-based classifications. They

identified a pixel-based Artificial Neural Network (ANN) as the best classifier [36]. The results from Abeysinghe et al. (2019) [36] indicated the importance of including a canopy height model (CHM) as a variable in the classification. Vegetation height is an important distinguishing characteristic for the in situ identification of *Phragmites* since it grows up to five meters tall. The importance of a CHM for remotely sensed identification of *Phragmites* has been corroborated by Anderson et al. (2021) [37]. Classification accuracies greater than 94% were attained in other studies when using ANNs [38,39]. In contrast, Mohler et al. (2022) concluded that different machine learning algorithms perform better than ANNs for *Phragmites* mapping [40], and results from Anderson et al. (2023) suggested that multiple machine learning algorithms perform similarly [41].

Results from these studies demonstrate that there has been no general consensus on the single, best machine learning algorithm for *Phragmites* mapping. A possible solution is a voting-based ensemble classifier that implements multiple machine-learning models to make predictions. Ensemble classifications have been used by others to predict the spatial extent of cover classes. Sachdeva et al. (2020) [42] compared a voting-based ensemble classifier to individual machine learning algorithms for predicting landslide susceptibility. They found that a voting-based ensemble classifier containing a logistic regression, gradient-boosting decision tree, and a Voting Feature Interval outperformed many individual machine learning algorithms, including Random Forest (RF), SVM, and ANN [42]. Higher classification accuracies when using a voting-based ensemble classifier compared to individual machine learning algorithms were also noted by Aguilar et al. (2018) [43] when mapping crop types in Africa. Other research has focused on mapping wetland types. Foody et al. (2007) applied a voting-based ensemble classifier to map fens. Their results demonstrated the capability of voting-based ensemble classifiers to map single cover classes with accuracies above 95% [44]. The aptitude of voting-based ensemble classifiers to map invasive wetland vegetation was explored by Liu et al. (2020) [45]. They found that the voting-based ensemble classifier implemented in their study was more transferable to new sites than a single SVM. Most research focused on mapping invasive *Phragmites* has concentrated on using a single machine learning algorithm to make predictions.

This study aimed to investigate the capability of a voting-based ensemble classifier for identifying invasive *Phragmites* within Minnesota wetlands. Three-band (red, green, blue; RGB) UAS imagery and five-band (red, green, blue, red edge, near-infrared; multispectral; MS) UAS imagery were classified using a voting-based ensemble classifier containing an RF, histogram-based gradient-boosting classification tree (HGB), and two ANNs. Classifications are then further refined using object-based image analysis (OBIA) techniques. The application of OBIA techniques after image objects were assigned an initial cover class from a machine learning algorithm, which allowed for the refinement of cover class extents using contextual information [41]. The objectives of this study were: (I) to explore the capability of a voting-based ensemble classifier for *Phragmites* identification; (II) to evaluate whether additional spectral bands, i.e., multispectral UAS imagery, more accurately identifies *Phragmites* compared to RGB UAS imagery; (III) to determine if a CHM is required to accurately map *Phragmites* while using multispectral imagery; and (IV) to assess the effects of using OBIA to refine voting-based ensemble classifications of *Phragmites*.

2. Materials and Methods

2.1. Study Area

Six wetland complexes located in Minnesota, USA, were used in this study (Figure 1). Minnesota experiences a humid continental climate. Average monthly temperatures range from −11 degrees Celsius in the winter to 23 degrees Celsius in the summer. Average annual precipitation varies from roughly 500 mm in northwest Minnesota to 900 mm in southeast Minnesota. Site A is the Delano wastewater treatment facility (WWTF) in Delano, Minnesota (Figure 2A). Vegetation at the Delano WWTF is fairly uniform. This site has two reed beds that have been planted with invasive *Phragmites* (Figure 3A). The two

reed beds are located in the northern and northeastern parts of the WWTF grounds. An escaped population of *Phragmites* was present along the perimeter of a small wetland to the southwest of the planted reed beds. However, this area was treated with herbicide in the fall of 2021. Living *Phragmites* stems were not growing in this wetland at the time of data collection. Instead, dead *Phragmites* was the dominant cover type within the wetland. Scattered patches of cattails (*Typha* sp.) were also present. A majority of the Delano WWTF is otherwise mowed grass with a few scattered trees.

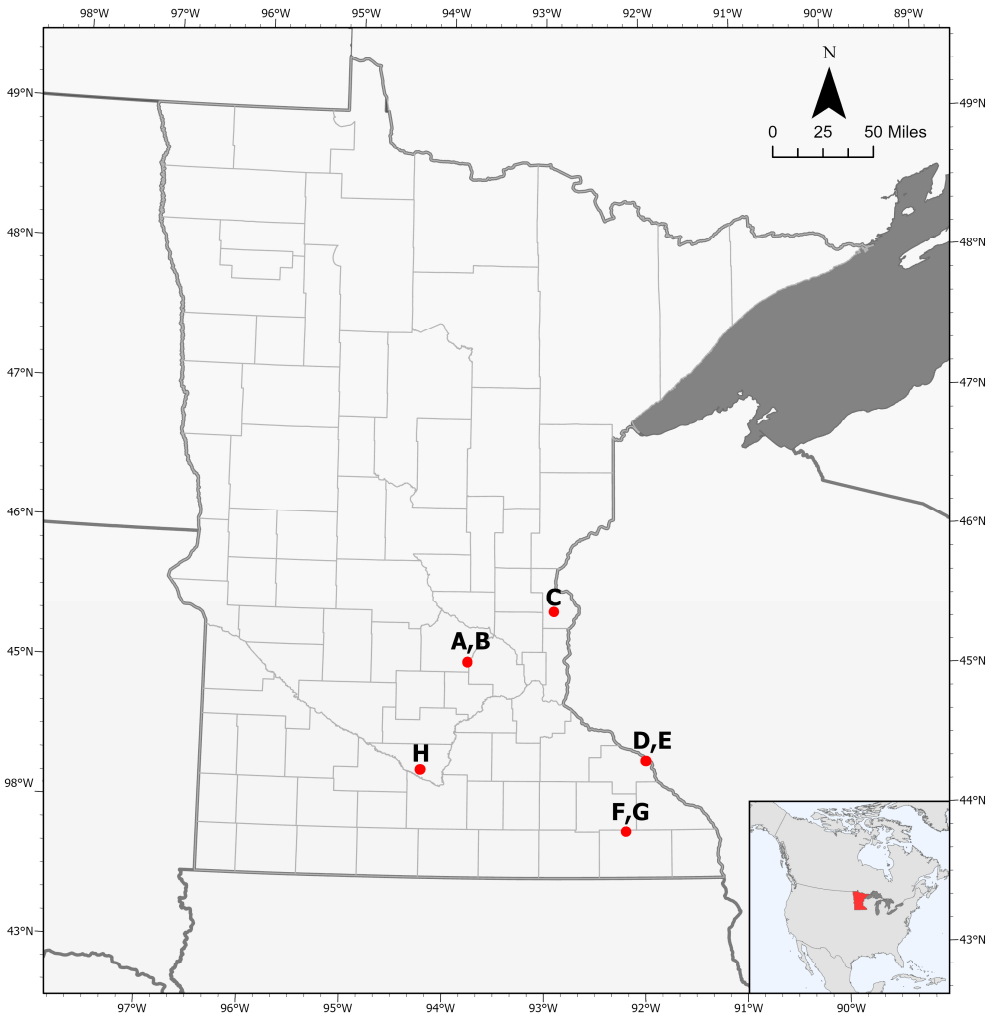


Figure 1. Study sites located in Minnesota, USA; (**A**) Delano wastewater treatment facility, (**B**) Delano City Park, (**C**) Chisago City property, (**D**) Wabasha property (2021), (**E**) Wabasha Property (2022), (**F**) Chatfield wastewater treatment facility (2021), (**G**) Chatfield wastewater treatment facility (2022), and (**H**) Swan Lake Wildlife Management Area.

Site B, the Delano City Park (Figure 2B), is located directly south of the Delano WWTF within a residential area. A sports complex is present to the west of the site, and residential housing borders the park to the northeast and southwest. The majority of the site is dominated by a wetland complex that is divided by a paved path. This site previously had multiple large patches of *Phragmites*. However, all *Phragmites* patches were treated with herbicide in the fall of 2021. A majority of the *Phragmites* present in 2021 was not present in 2022. However, a few small patches of *Phragmites* remain near the treated patches (Figure 3B). These remaining patches of *Phragmites* have low stem densities. Non-*Phragmites* herbaceous vegetation dominates a majority of the study area. Reed canary grass (*Phalaris arundinacea*) and cattails are the prevailing species.

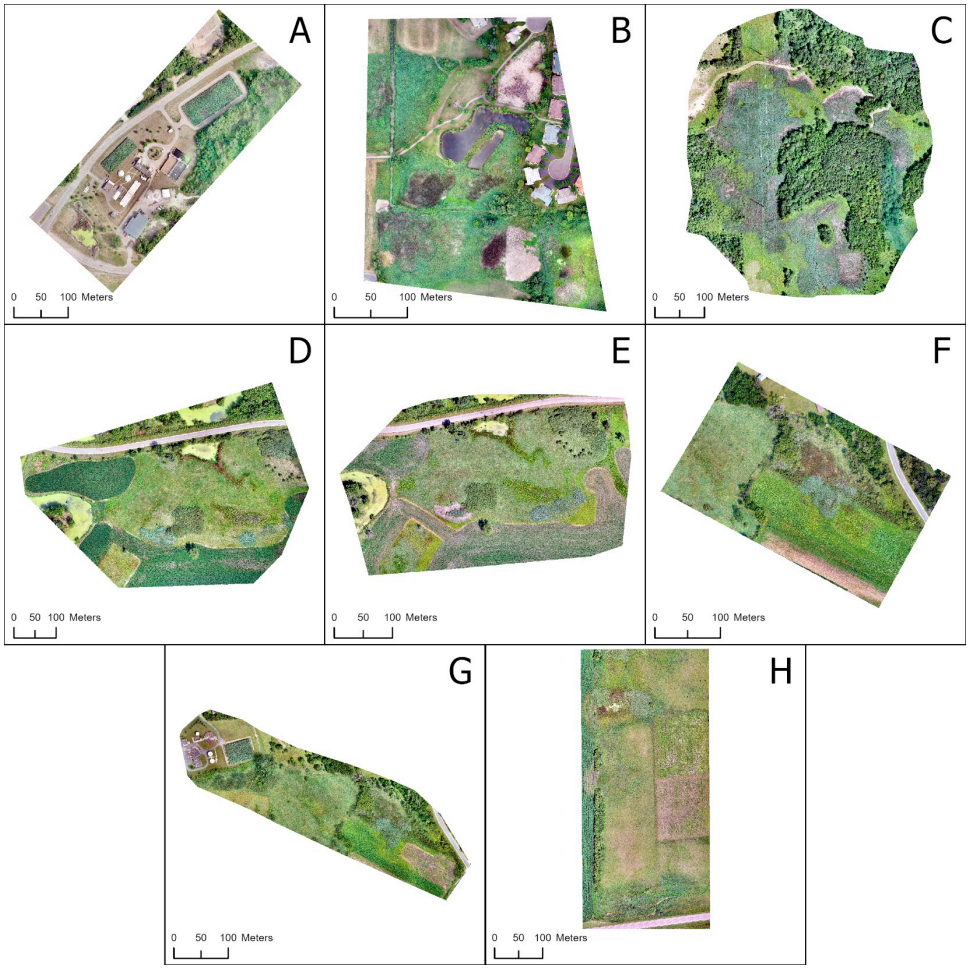


Figure 2. RGB orthomosaics for each study site: (**A**) Delano wastewater treatment facility, (**B**) Delano City Park, (**C**) Chisago City property, (**D**) Wabasha property (2021), (**E**) Wabasha Property (2022), (**F**) Chatfield wastewater treatment facility (2021), (**G**) Chatfield wastewater treatment facility (2022), and (**H**) Swan Lake Wildlife Management Area.

Site C resides on private property near Chisago City, Minnesota (Figure 2C). This study area is a large wetland complex located to the south of the Sunrise River. Water flows through a small tributary of Sunrise River through the wetland complex. Site C is surrounded by agricultural fields consisting mostly of row crops and hay fields. *Phragmites* is the dominant, non-woody species within the study site (Figure 3C). Despite the abundance of *Phragmites*, a variety of native grasses, sedges, rushes, and flowers are present within the wetland portions of the site. Large stands of trees and scattered shrubs are present within the site.

Sites D and E are separate acquisitions over the same private property near Wabasha, Minnesota (Figure 2D,E). The property is located adjacent to the Upper Mississippi River National Wildlife and Fish Refuge (United States Fish and Wildlife Service) and the Pool 4 Wildlife Management Area (Minnesota Department of Natural Resources). Row crops are present along the eastern, southern, and western edges of the site. Reed canary grass is the dominant species within the site. *Phragmites* distribution within the site changed between 2021 (Figure 3D) and 2022 (Figure 3E). In 2021, seven *Phragmites* patches were present within the site (Figure 3D). Three patches were growing on the western side of the site between the two agricultural fields. A single, large patch was growing next to a large stand of willows (*Salix* sp.) in the center of the study area. Two patches were present immediately north of the soybean field on the eastern side of the site. Lastly, a patch of *Phragmites* was north of the roadway. This patch consisted of a few scattered stems, and it

was entirely obscured by the tree canopy. The extent of *Phragmites* changed considerably by 2022. The three patches on the western side of the site were replaced by a two-track access road running between the agricultural fields. Herbicide was used to treat the large patch in the center of the site during the fall of 2021. A living portion of the patch next to the willow stand still remains. The two patches on the eastern side of the site grew together to form a single, large patch. Multiple small clumps of *Phragmites* are present on the periphery of this larger patch. The patch north of the roadway has expanded, and the stem density has increased.

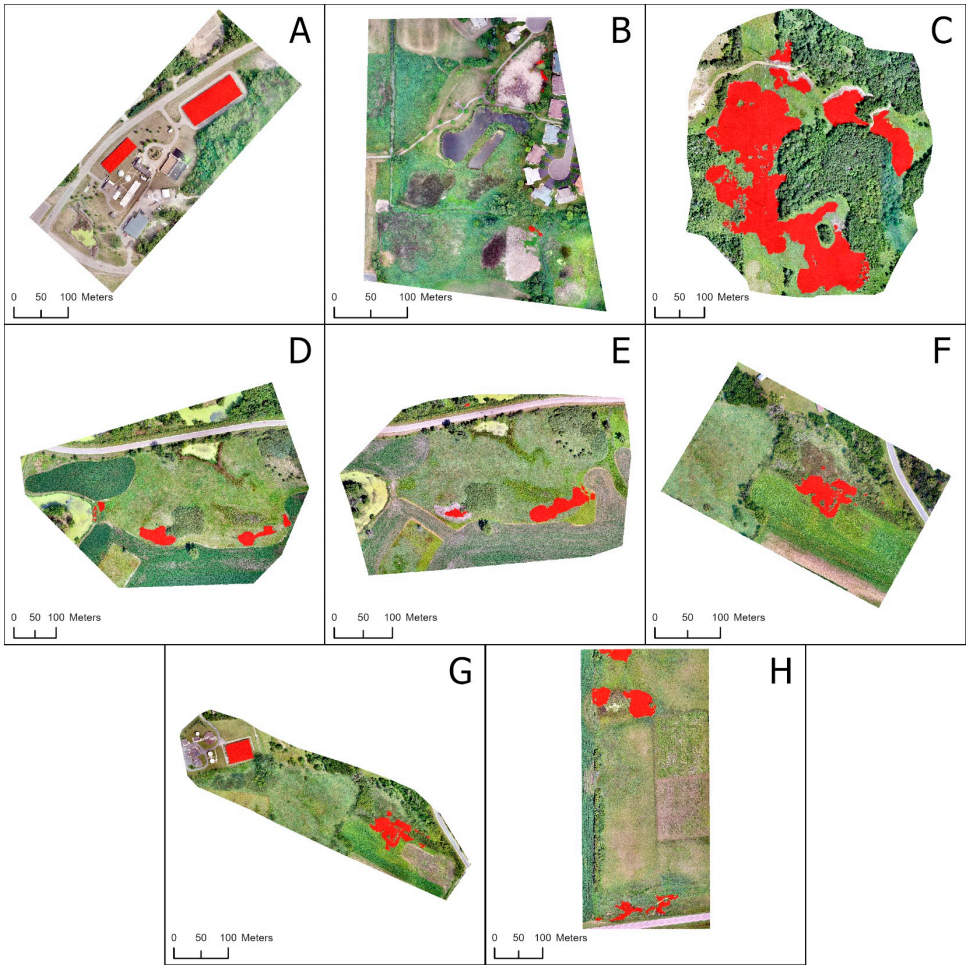


Figure 3. Location of *Phragmites* within each study site (highlighted in red): (**A**) Delano wastewater treatment facility, (**B**) Delano City Park, (**C**) Chisago City property, (**D**) Wabasha property (2021), (**E**) Wabasha Property (2022), (**F**) Chatfield wastewater treatment facility (2021), (**G**) Chatfield wastewater treatment facility (2022), and (**H**) Swan Lake Wildlife Management Area.

Similar to Sites D and E, Sites F and G are separate acquisitions over the same study area located in Chatfield, Minnesota (Figure 2F,G). This study area contains the Chatfield WWTF and portions of the adjacent private property. Two water bodies border the WWTF. Mill Creek runs to the west, and the north branch of the Root River runs to the west and south. Planted and escaped populations of *Phragmites* are present at this site (Figure 3F,G). The city of Chatfield operates a single reed bed planted with invasive *Phragmites*. *Phragmites* from this reed bed has spread to the neighboring property, and satellite populations have become established. A single, large patch surrounded by multiple, smaller patches is present on the eastern side of the study site. By 2022, the multiple escaped populations had expanded radially. The expansion consisted of both an increase in high stem density areas and the establishment of individual scattered stems surrounding the large patch. The

land to the east of the WWTF contains herbaceous wetland vegetation, scattered stands of willows, and stands of sumac (*Rhus* sp.).

Site H is the Swan Lake Wildlife Management Area (WMA): Nicollet Bay Main Unit located near Nicollet, Minnesota (Figure 2H). The majority of the study area is a restored, tall grass prairie. Common grass species include big bluestem (*Andropogen gerardii*) and Indian grass (*Sorghastrum nutans*). Non-restored areas consist of a reclaimed agricultural field on the eastern side of the site and an active agricultural field on the western edge of the site. Seasonally flooded wetlands are also present along the roadway at the southern edge of the site as well as north of the reclaimed agricultural field. Reed canary grass is common within these areas. Populations of invasive *Phragmites* are present within the Swan Lake WMA along the road at the southern end of the site (Figure 3H). Native *Phragmites* populations are present in the northern half of the site as well. One patch is located at the far northern edge next to a stand of sumac. Two other patches are growing on the eastern and western sides of a seasonally flooded basin. The native *Phragmites* within this study area is growing as dense and as tall as the invasive *Phragmites* found near the roadway.

2.2. Image Processing

2.2.1. Optical Imagery

The imagery was acquired between July and August of 2021 and 2022 (Table 1). Acquisition dates corresponded to the time when *Phragmites* had reached maximum height for the summer. Each of the six study sites was flown with a Microdrones MD4-1000. Images were acquired over multiple flights using two different sensors. First, the vehicle was equipped with a Sony Rx1RII camera and an Applanix APX-15 IMU fitted to a gravity (nadir) gimbal. This sensor collected data in the red, green, and blue spectrums (i.e., RGB). Flights with the RGB sensor were flown at about 121 m above ground level, and images were collected with 85% endlap and 70% sidelap. The resulting imagery had a ground sampling distance between 1.5 to 1.7 cm. The second sensor was a Micasense RedEdge MX multispectral camera that collected image data in the red (668 nm), green (560 nm), blue (475 nm), red edge (717 nm), and near-infrared (842 nm) spectrums. Images were manually captured over a calibration reflectance panel pre-flight to allow for the calculation of reflectance values. Flights with the multispectral sensor were flown at about 121 m above ground level, and images were acquired with 75% endlap and sidelap. The resulting imagery had a ground sampling distance between 7.5 to 8.8 cm.

Table 1. UAS collections at each study area. All RGB imagery (red, green, and blue spectral bands) was acquired at 121 m above ground level with 85% endlap and 70% sidelap. All multispectral (MS) imagery was acquired at 121 m above ground level with 75% endlap and sidelap.

Study Area	Collection Date	Hectares	RGB Resolution	MS Resolution	Weather
Delano WWTF	15 July 2022	10.8	1.68 cm	8.7 cm	Partly cloudy and light wind
Delano City Park	15 July 2022	11.0	1.7 cm	8.8 cm	Partly cloudy and light wind
Chisago City	21 July 2022	23.4	1.66 cm	8.4 cm	Partly cloudy and moderate wind
Wabasha	12 August 2021	11.6	1.66 cm	8.6 cm	Clear skies and moderate wind
Wabasha	4 August 2022	11.3	1.5 cm	7.5 cm	Clear skies and light wind
Chatfield WWTF	3 August 2021	8.6	1.61 cm	8.4 cm	Clear skies with light haze from wildfire smoke
Chatfield WWTF	2 August 2022	13.2	1.5 cm	7.3 cm	Clear skies and moderate wind
Swan Lake WMA	19 July 2021	15.5	1.68 cm	8.8 cm	Mostly clear and light wind

The Microdrones MD4-1000 used for the acquisitions had post-processing kinematic capabilities when equipped with the RGB sensor and Applanix APX-15 IMU. The Minnesota Department of Transportation-managed Continuously Operating Reference Stations (CORS) network was used for the GNSS post-processing. Base station files from the nearest CORS station to each study area were used within the Applanix POSPac software (v. 8.6) to correct the multi-frequency GNSS from the UAS and georeference the RGB imagery. An orthomosaic image, a three-dimensional point cloud, and a digital surface model were computed from the georeferenced RGB imagery using Pix4Dmapper [46]. All data layers were projected into UTM WGS84 Zone 15N referencing the EGM96 geoid. Visual interpretation of the RGB orthomosaics indicated good matching between images with minimal motion blur caused by moving vegetation. Digital surface models for each study site were used as produced by Pix4Dmapper, except for the Chisago City site. The Chisago City site has a high-voltage powerline that goes through the site. This resulted in the creation of points on the wires between support towers. Quick Terrain Modeler [47] was used to manually remove points created on the powerlines and produce a new digital surface model.

Post-processing kinematics was not employable while using the Micasense RedEdge MX multispectral sensor. The multispectral images were processed using Pix4Dmapper to create a mosaic image in the same projected coordinate system as the RBG data layers. Spectral values of the imagery were converted to reflectance during the Pix4Dmapper processing pipeline using the images acquired over the calibration reflectance panel. Similar to the RGB orthomosaics, visual interpretation of the multispectral mosaics indicated good image matching with minimal motion blur. Ground control points were established throughout each study site pre-flight using an Emlid RS2 multifrequency receiver in order to align the multispectral mosaic image to the RGB orthomosaic image. The Emlid receiver was used as a real-time kinematic rover for real-time GNSS measurement and data collection. Control points were used to georeference the multispectral imagery to the RGB imagery using the Georeferencing tools in ESRI's ArcGIS Pro [48]. The Georeferencing tools in ArcGIS Pro require a minimum of three control points. However, the Swan Lake WMA site, the 2021 collection of the Chatfield WWTF, and the 2022 collection of the Wabasha site did not meet this requirement. Easily discernable features within both the RGB and multispectral imagery were identified and manually selected as control points to be used for georeferencing. Examples of identifiable features include large rocks, road markings, and manhole covers.

A portion of the 2021 Wabasha study area was removed from the RGB and multispectral orthomosaics. The removed area contained a segment of the neighboring cornfield. This area was removed from the orthomosaics because the total area of corn was not large enough to support the effective training of a corn class with a machine-learning classifier.

2.2.2. Lidar

A lidar dataset is available for Minnesota through MnTOPO (http://arcgis.dnr.state.mn.us/maps/mntopo/ (accessed on 1 September 2021)). Lidar data were acquired over the six study sites between 2007 to 2010 during the spring or fall leaf-off periods (Table 2). Although *Phragmites* remains standing year-round, it has less aboveground biomass outside of the growing season. This allowed the laser to better circumvent the vegetative canopy and interact with the ground surface. Visual interpretation of the lidar point clouds confirmed that vegetation returns were not being incorrectly classified as ground returns within our study areas. Classified ground points were used to create a digital elevation model for each study area. Creation of the digital elevation models was completed using rapidlasso LAStools [49], and the resulting digital elevation models had a spatial resolution of 1.0 m^2. The Minnesota lidar data were originally projected in UTM NAD83 Zone 15N while using the North American Vertical Datum of 1988 (NAVD88) referencing Geoid09. The raster DEMs were reprojected using the Geospatial Data Abstraction Library (GDAL) [50] to UTM WGS84 Zone 15N referencing the EGM96 geoid.

Table 2. Lidar collection periods for each study area.

Study Area	County	Collection Period
Delano WWTF	Wright	23 April–28 May 2008
Delano City Park	Wright	23 April–28 May 2008
Chisago City	Chisago	18–28 April 2007
Wabasha	Wabasha	18–24 November 2008
Chatfield WWTF	Olmsted	18–24 November 2008
Swan Lake WMA	Nicollet	8 April–5 May; 2–19 November 2010

2.3. Classification

An OBIA workflow with a voting-based ensemble classifier was selected for this study (Figure 4). Object-based image analysis workflows begin by using a pairwise matching scheme to group pixels with similar spectral and textural values [51]. Classification of these groups of pixels, or image objects, allows for the incorporation of size, shape, and contextual information of image objects as well as their spectral and textural information for feature identification. Object-based classifications frequently result in better approximations of real-world features compared to pixel-based classifications [52,53]. Machine learning algorithms are commonly used to classify image objects created from a single segmentation scale. However, this does not allow for the inclusion of contextual information within a classification workflow, such as those using hierarchical segmentation schemes [54] or post-processing machine learning classifications using object-based rule sets (post-machine learning OBIA rule set; post-ML OBIA rule set) [41]. Previous research has indicated that post-ML OBIA rule sets can improve classification accuracies of *Phragmites* [41]. This study employed a post-ML OBIA rule set to refine voting-based ensemble classifications.

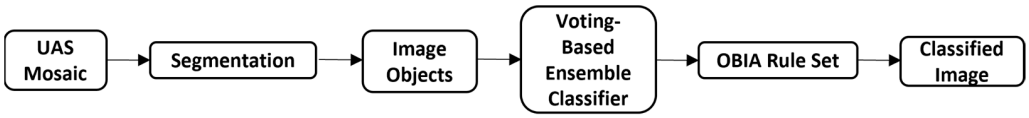


Figure 4. Classification workflow used in this study. The UAS mosaic was segmented to produce image objects, the image objects were classified using a voting-based ensemble classifier, and then the classified objects were further refined using a post-ML OBIA rule set within the Trimble eCognition Developer software (v. 10.2).

One challenge when using machine learning to classify an image is determining which machine learning algorithm to use. Others have investigated which machine learning algorithm produces the best results, and results vary between studies [36,55–58]. This study uses an ensemble of three different machine learning algorithms to classify image objects: RF, HGB, and ANN. Final predictions are assigned based on the majority vote from each of the classifiers within the ensemble. Voting-based ensemble classifiers remove the need to choose a single machine learning algorithm, and they have been used successfully by others for image classification [42–45,59].

2.3.1. OBIA Workflow

Two OBIA workflows were used in this study: (1) A workflow to classify the RGB imagery (hereafter RGB workflow); and (2) A workflow to classify the multispectral imagery (hereafter multispectral workflow). Each OBIA workflow was created using a combination of the Trimble eCognition Developer software [60] and Python [61]. The RGB workflow used the workflow established in [41]. However, there were two differences between the workflow published by Anderson et al. (2023) [41] and the RGB workflow employed in this study. First, the voting-based ensemble classifier described herein was used to assign the initial cover class. Second, the green-blue ratio parameter was computed and exported with the image objects for use in the voting-based ensemble classification. The formula for this parameter is discussed below. Otherwise, the same rule sets were used for the RGB

workflow in this study to create image objects and to post-process the machine learning classifications of *Phragmites*.

The multispectral workflow began by loading the image layers into eCognition and creating ten temporary raster layers. First, a normalized digital surface model was created by differencing the UAS-derived digital surface model from the lidar-derived digital elevation model. The term canopy height model (CHM) is used synonymously with the normalized digital surface model hereafter. Second, the visible atmospherically resistant index (VARI) was created. VARI estimates vegetation fraction, and it has been employed by others for identifying *Phragmites* from UAS imagery [62]. This index was calculated using the following formula:

$$\frac{green - red}{green + red - blue}$$

The third normalized difference vegetative index (NDVI), fourth normalized difference red edge index (NDRE), and fifth visible-band difference vegetative index (VDVI) [63] temporary layers are estimates of the amount of chlorophyll within plants. NDVI was calculated using the following formula:

$$\frac{nir - red}{nir + red}$$

NDRE was computed using the following formula:

$$\frac{nir - rededge}{nir + rededge}$$

VDVI was calculated using the following formula:

$$\frac{(2 * green) - red - blue}{(2 * green) + red + blue}$$

The sixth temporary layer generated was the normalized difference between the red and blue spectral bands (red-blue ratio). It was noticed in previous work that the blue spectral band exhibited lower values over woody vegetation than over *Phragmites*, and this spectral index highlighted that difference [41]. The red-blue ratio was calculated using the following formula:

$$\frac{red - blue}{red + blue}$$

Visual interpretation of the multispectral imagery revealed a small difference in the green spectral band between *Phragmites* and non-*Phragmites* herbaceous vegetation while having similar values in the blue spectral band. A normalized difference between green and blue spectral bands (green-blue ratio) was computed in an attempt to emphasize this difference. The green-blue ratio was computed using the following formula:

$$\frac{green - blue}{green + blue}$$

Lastly, three temporary layers were created only for their use in the multi-resolution segmentation. Pix4Dmapper scales the reflectance values and converts them to 32 bit floating point by default during the creation of the reflectance images. eCognition's multi-resolution segmentation does not operate efficiently on image layers where raster cell values are very small decimals. The red, green, and blue spectral bands were multiplied by 100,000 and then converted to 16-bit integers to be used for the multi-resolution segmentation.

The multispectral imagery was then segmented within eCognition using the multi-resolution segmentation algorithm with the 16-bit versions of the red, green, and blue spectral bands as input. Multi-resolution segmentation initially categorizes individual pixels as separate segments. Individual segments are then merged pairwise into larger

segments using a user-defined threshold [51], i.e., the scale parameter. Segments are merged if the increase in heterogeneity is less than the threshold. Larger values for the scale parameter result in larger image objects. Two additional parameters are required for the multi-resolution segmentation: shape and compactness. The shape parameter controls the influence of shape compared to color during image object creation. Higher values give more control to shape in the creation of image objects than color. Smaller values for the shape parameter result in a greater influence of color than shape during image object creation. Compactness determines the smoothness or compactness of an image object. For example, lower values for compactness will create smooth image objects, while higher values will produce more condensed image objects. A scale parameter value of 100, a shape parameter value of zero, and a compactness value of one were used for the multi-resolution segmentation of the multispectral imagery. These parameter values were determined to be optimal through trial and error. Objects created from the multi-resolution segmentation were exported and classified by the voting-based ensemble classifier in Python. Six cover classes were predicted: *Tree*, *Short Tree*, *Wetland Vegetation*, *Mowed Grass*, *Agriculture*, and *Phragmites*.

Image objects were subjected to another OBIA workflow in eCognition once they were ascribed an initial class by the voting-based ensemble classifier. This post-ML OBIA rule set began by using the NDVI image layer to remove all image objects that did not contain vegetation. Image objects with an NDVI less than 0.15 were assigned to the *Not Vegetation* cover class. Next, scattered individual objects breaking up continuous sections of a single cover class were fixed. This was completed by using the Relative Border To rule. This rule identifies each image object's neighboring image objects, and it computes the percentage of its border shared by each cover class. A high threshold of 0.8, or 80%, was used to reassign scattered image objects to the cover class they shared 80% of their border with.

Phragmites false positives were corrected after the removal of scattered, individual image objects. First, all *Phragmites* image objects with a mean VDVI value of less than 0.1 were assigned to the *Scratch* class. The *Scratch* class is a temporary cover class used throughout the post-ML OBIA rule set to temporarily hold image objects before reassignment to their final cover class. The 25th and 90th quantiles of CHM values within an image object were also used to remove *Phragmites* image objects that contained vegetation too short to be *Phragmites*. Objects with a 25th CHM quantile value of less than 0.75 m and a 90th CHM quantile value of less than 1.4 m were assigned to the *Scratch* class. Objects within the *Scratch* class were reassigned to the *Tree* class if they shared 50% of their border. Those that shared 50% of their border with the *Wetland Vegetation* class were reassigned to the *Wetland Vegetation* class. Next, shorter trees intermixed within *Phragmites* patches were removed using the Red-Blue ratio image layer. *Phragmites* objects with a Red-Blue ratio value greater than 0.1 were reclassified based on their shared border to other cover classes. Objects were first moved to the *Tree* class if they shared any portion of their border with the *Tree* class. The remaining *Phragmites* with a Red-Blue ratio value greater than 0.1 were moved to the *Wetland Vegetation* class if they shared any part of their border with the *Wetland Vegetation* class. This continued for the *Short Tree*, *Agriculture*, *Lawn*, and *Scratch* cover classes.

Dead non-*Phragmites* vegetation that was originally removed using the NDVI image layer was then reassessed. It was noted that correctly classifying dead vegetation within a *Phragmites* patch resulted in a more successful application of the Relative Border To rule for refining *Phragmites* patch boundaries. Image objects in the *Not Vegetation* class were reassigned to the *Tree* class if they shared 80% of their border. The same was computed for *Not Vegetation* image objects sharing a boundary with the *Wetland Vegetation* class. *Not Vegetation* image objects sharing 33% of their border with the *Tree* class while also possessing a mean CHM value greater than two meters were reassigned to the *Tree* class. Lastly, to refine the *Tree* cover class, image objects within the *Scratch* class were moved to the *Tree* class if they shared 50% of their border.

The post-ML OBIA rule set then focused on fixing misclassification between the *Tree*, *Short Tree*, and *Phragmites* cover classes. Trees misidentified as *Phragmites* objects were reassigned to the *Tree* class if they had a Red-Blue value greater than 0.1, shared more than 33% of their border with *Tree* objects, and had an area of less than 200,000 pixels. All individual objects in the *Short Tree* cover class were then merged together to create a smaller number of larger image objects. The remaining *Short Tree* objects that had a 90th CHM quantile of less than 4.5 m, a 25th CHM quantile greater than 0.5 m, and a mean Red-Blue ratio less than 0.15 were assigned to the *Scratch* class. Image objects within the *Scratch* class were then assigned to the *Phragmites* class if they had a mean CHM value greater than one meter and a mean Red-Blue ratio value less than 0.1. Next, *Phragmites* objects that had a shared border with the *Tree* class of greater than 90% were assigned to the *Tree* class. Objects meeting this requirement generally were found at the edges of tree canopies that neighbored *Phragmites* patches. *Short Tree* objects were then assigned to the *Phragmites* class if they had a Red-Blue ratio of less than 0.1, a 50th CHM quantile value less than five meters, and a shared border with *Phragmites* objects greater than 33%.

Further refinement of the *Short Tree-Tree-Phragmites* relationship was completed using the Relative Border To rule and the Red-Blue ratio image layer. *Phragmites* objects with a Red-Blue ratio of greater than 0.2 or those that shared more than 90% of their border with *Short Tree* objects were assigned to the *Scratch* class. Objects within the *Scratch* class were then assigned to the *Short Tree* class if they shared more than 50% of their border. Similarly, image objects within the *Scratch* class were assigned to the *Tree* class if they shared more than 80% of their border.

The last series of rules was designed as a final attempt to refine the *Phragmites* cover class. *Phragmites* objects that shared 60% or more of their border with the *Not Vegetation* class were reassigned to that class. The *Short Tree* class was merged together with the *Tree* class, and *Phragmites* objects were reassigned to the *Tree* class if they shared at least 75% of their border. The last rule utilizing neighboring image objects assigned any image objects within the *Scratch* class sharing more than 50% of their border to *Phragmites* objects to the *Phragmites* class. Four concluding rules were used as a final filter for *Phragmites* commission errors. *Phragmites* that had either a mean VDVI value greater than 0.05, less than 5000 pixels in area, a mean CHM value less than 1.5 m, or a 90th CHM quantile value greater than 4.25 m were assigned to the *Scratch* class. All image objects not assigned to the *Phragmites* class were merged together and reassigned to the *Not Phragmites* class. The resulting classification had two cover classes, *Phragmites* and *Not Phragmites*.

2.3.2. Voting-Based Ensemble Classifier

Classification of the image objects was completed using a voting-based ensemble classifier with the Scikit-Learn Python package [64]. Three voting-based ensemble classifiers were created for this study: (1) Using the RGB imagery with the CHM derived from the RGB imagery (RGB classifier); (2) Only using the multispectral imagery (MS classifier); and (3) Using the multispectral imagery with the CHM derived from the RGB imagery (MS/CHM classifier). The only pre-training difference between the MS classifier and the MS/CHM classifier was the addition of a CHM and the associated parameters. The creation of the two multispectral voting-based ensemble classifiers was completed to determine the impact of including a CHM within a multispectral classification. Incorporating an RGB voting-based ensemble classifier permitted inference on the influence of the additional spectral bands for identifying *Phragmites*.

A pipeline was implemented in Python to preprocess and classify the image objects. Classification of the image objects was completed using a voting-based ensemble classifier containing an RF, HGB, and two ANNs. Each of these algorithms has been widely used individually for land cover classification and invasive species mapping [65–67]. The first step in the pipeline was to standardize each parameter. This was completed by subtracting the mean value of a parameter from each sample and dividing it by the parameter's standard deviation. Next, a Principal Component Analysis (PCA) was applied to the

standardized data to reduce the number of parameters. Selection of the final number of principal components was automated through the Minka's maximum likelihood estimator (MLE) [68] option in the Scikit-Learn PCA tool. The Minka's MLE uses Bayesian model selection to estimate the dimensionality of the input data and select the most appropriate number of principal components [68]. A total of 23 principal components were selected by the Minka's MLE option for the RBG classifier, 26 principal components were selected for the MS classifier, and 21 principal components were selected for the MS/CHM classifier. Image objects were classified using a voting-based ensemble classifier after the completion of the pre-processing steps. All image objects were classified using each of the aforementioned machine learning classifiers, and the probabilities of an object being in each class were calculated. The probabilities for each cover class were then summed across each machine-learning algorithm. Whichever cover class had the highest summed probability was assigned to the image object. The scikit-learn implementations for each of these three algorithms were used [64]. Five-hundred estimators and the remaining default options were used within the RandomForestClassifier. The Scikit-Learn implementation of an HGB (HistGradientBoostingClassifier) uses a logistic loss function, a learning rate of 0.1, and a maximum of 31 leaf nodes by default. We elected to increase the maximum number of leaf nodes to 500 while maintaining the remaining default options. The Scikit-Learn MLPClassifier, or multi-layer perceptron classifier, was used for both the ANNs. This ANN uses a rectified linear unit function as an activation function and the Adam stochastic gradient-based optimizer [69]. A single hidden layer with 100 neurons was used for the first ANN, and the second ANN had two hidden layers, both with 100 neurons. All other parameters for the MLPClassifier were the default options. The parameters used for each algorithm (RF, HGB, and ANN) were selected through trial and error during the training phase.

2.4. Training and Validation

2.4.1. Model Training

Three of the eight collections were selected for training, including Delano WWTF, the 2021 collection of the Wabasha property, and the 2022 Chatfield WWTF collection. These collections were selected due to: (1) The *Phragmites* in the WWTF reed beds providing large, continuous patches of *Phragmites*; (2) Validation of the classifier using the WWTF reed beds being impractical because the *Phragmites* is within a managed environment; and (3) Each cover class needing to be adequately represented across the three training sites.

Training data for each cover class were created by manually digitizing polygons at each training site using their corresponding RGB UAS orthomosaic. Accessibility was limited at each of the study sites. This excluded the use of a handheld Global Positioning System unit for polygon delineation. Each site was navigated to the extent possible prior to image acquisition in order to determine the distribution of cover classes within the site. Field knowledge and image interpretation were combined to accurately digitize cover class boundaries. Delineating the exact boundary of a *Phragmites* patch can be difficult due to reduced *Phragmites* stem density near the edges of a patch. The *Phragmites* polygons digitized for this study required a complete *Phragmites* canopy cover to be included within the training polygons. This excluded scattered *Phragmites* stems intermixed with non-*Phragmites* vegetation near the periphery of *Phragmites* patches. Training polygons for the five non-*Phragmites* cover classes were manually digitized, including *Agriculture*, *Mowed Grass*, *Wetland Vegetation*, *Tree*, and *Short Tree*. Shorter trees, such as willows and sumac, were included within the *Short Tree* cover class. Only herbaceous wetland vegetation was included in the *Wetland Vegetation* class.

Two sets of image objects were created using the training polygons. First, image objects were created for the multispectral classifications using the multispectral UAS imagery (Table 3). A multi-resolution segmentation in eCognition was employed using the same parameters as discussed in the *Classification* section. Multispectral training objects were exported and used to train the MS classifier and the MS/CHM classifier. Twenty-

nine parameters were included for the MS classifier prior to the PCA (Table 4). Thirty-six parameters were included in the MS/CHM classifier training data prior to the PCA. The brightness parameter is an estimate of an object's overall brightness [70]. White objects have higher brightness values compared to black objects. Edge contrast evaluates the pixel values of an image layer that neighbors an image object and contrasts those values to the mean image layer value within the image object [70]. A window size of 10 was selected for computing the edge contrast for the blue, green, red, near-infrared, red edge, CHM, and NDVI image layers. Image texture has been identified as an important parameter for the identification of *Phragmites* from UAS imagery [34]. Grey-level co-occurrence matrix (GLCM) homogeneity and contrast were calculated for each image object [71]. These two GLCM values highlight areas with similar and dissimilar image textures. Maximum difference measures the difference between an image object and its neighboring objects across all image layers [70]. Lastly, two categorical variables were computed: Tall Bitmask and Short Bitmask. These two binary parameters (0, 1) categorized an image object as tall or short. Image objects with a mean CHM value greater than five meters were assigned a value of one for the Tall Bitmask parameter, while image objects with a mean CHM value below five meters were assigned a value of zero. The Short Bitmask layer highlighted shorter vegetation. Image objects with a mean CHM value less than one meter were assigned a one for the Short Bitmask parameter, and image objects with a mean CHM value greater than or equal to one were assigned a value of zero. It was noticed during ensemble creation that these two parameters limited the commission errors for the *Tree* and *Mowed Grass* cover classes.

Table 3. Number of training image objects per cover class for the multispectral classification (MS) and RGB (red, green, and blue spectral bands) classification. Training samples were created using the multi-resolution segmentation in the Trimble eCognition Developer software. The RGB and MS training samples cover the same spatial extent, but the number of training samples per cover class varies due to different multi-resolution segmentation parameters.

Classification Type	Cover Class					
	Mowed Grass	***Phragmites***	**Tree**	**Short Tree**	**Wetland**	**Agriculture**
RGB	9597	93,744	49,061	24,044	258,554	130,773
MS	68,546	294,178	111,684	58,093	809,093	198,417

The second set of training image objects was generated for the RGB classification (Table 3). A multi-resolution segmentation in eCognition was applied to the RGB UAS collections using a scale parameter of 50, a shape value of 0.3, and a compactness value of 0.5. RGB training objects were exported and used to train the RGB classifier. Twenty-seven parameters were included within the training data prior to the PCA. Fewer available spectral bands in the RGB UAS imagery reduced the number of parameters for the voting-based ensemble classifier. The visible-band difference vegetation index (VDVI) was included within the RGB classification. This index is an estimate of plant health, similar to NDVI [63].

Training of each ensemble classifier (RGB, MS, MS/CHM) started with separating the training image objects into train and test datasets. Ninety percent of the training image objects were randomly selected for training the classifiers, while the remaining ten percent were used to test the classifiers. All objects within the training dataset were used to train the RF, HGB, and both ANNs. The combination of parameters that resulted in the highest classification accuracy of the test dataset was selected for use in the final classifier. The selection of parameters was completed through trial and error. The post-ML OBIA rule set for the multispectral data was created once the voting-based ensemble classifiers had been established. Each multispectral orthomosaic associated with the training sites was segmented and classified using the MS/CHM classifier. The classified multispectral orthomosaics were used to produce the eCognition rule set discussed in Section 2.3.1. This

study reused the post-ML OBIA rule described in [41] to post-process the RGB classifier classifications. Results from the training phase were: (1) An eCognition rule set to create image objects from the multispectral UAS orthomosaics; (2) Three voting-based ensemble classifiers trained to identify *Phragmites* (RGB, MS, MS/CHM); and (3) an eCognition rule set designed to refine the MS/CHM classifications.

Table 4. Parameters included for the classification using the RGB UAS imagery (RGB classifier), the multispectral classification without a canopy height model (MS classifier), and the multispectral classification with a canopy height model derived from the RGB UAS imagery (MS/CHM classifier).

Parameter	RGB Classifier	MS Classifier	MS/CHM Classifier
Brightness	X	X	X
Edge Contrast of Blue Band (Window: 10)	X	X	X
Edge Contrast of Green Band (Window: 10)	X	X	X
Edge Contrast of NDVI (Window: 10)		X	X
Edge Contrast of NIR Band (Window: 10)		X	X
Edge Contrast of CHM (Window: 10)	X		X
Edge Contrast of Red Band (Window: 10)	X	X	X
Edge Contrast of Red Edge Band (Window: 10)		X	X
Grey-Level Co-occurrence Matrix: Contrast	X	X	X
Grey-Level Co-occurrence Matrix: Homogeneity	X	X	X
Maximum Difference	X	X	X
Mean of Blue Band	X	X	X
Mean of Green Band	X	X	X
Mean of Green-Blue Ratio	X	X	X
Mean of NDRE		X	X
Mean of CHM	X		X
Mean of NDVI		X	X
Mean of NIR Band		X	X
Mean of Red Band	X	X	X
Mean of Red-Blue Ratio	X	X	X
Mean of Red Edge Band		X	X
Mean of VARI	X	X	X
Mean of VDVI	X		
Short Bitmask	X		X
Standard Deviation of Blue Band	X	X	X
Standard Deviation of Green Band	X	X	X
Standard Deviation of NDRE		X	X
Standard Deviation of CHM	X		X
Standard Deviation of NDVI		X	X
Standard Deviation of NIR Band		X	X
Standard Deviation of Red Band	X	X	X
Standard Deviation of Red-Blue Ratio	X	X	X
Standard Deviation of Red Edge Band		X	X
Standard Deviation of VARI	X	X	X
Standard Deviation of VDVI	X		
25th Quantile of CHM	X		X
90th Quantile of CHM	X		X
Tall Bitmask	X		X

2.4.2. Model Validation

The five collections not selected for the training phase were used to validate the voting-based ensemble classifiers (Figure 5). These collections include the 2021 acquisitions of the Swan Lake WMA and Chatfield WWTF and the 2022 acquisitions of the Chisago City property, the Wabasha property, and the Delano City Park. Validation points were generated using a multistep process. The validation process began by navigating each site to the extent possible to determine the location of *Phragmites* patches. Field knowledge was combined with available EDDMapS GIS data and image interpretation to digitize rough boundaries

around each *Phragmites* patch. As stated previously, identification of a patch boundary was difficult due to the reduced *Phragmites* stem density at the expanding edge of a *Phragmites* patch. Rough boundaries encompassed the expanding edge containing low stem density *Phragmites* and non-*Phragmites* vegetation. One hundred and fifty random points were then generated within the digitized boundaries for each validation site. The generation of validation points was completed using ESRI's ArcGIS Pro software (v. 3.0.2) [48]. Each of the *Phragmites* validation points was verified through manual image interpretation. Points were excluded from the validation set if they did not fall on a *Phragmites* plant. Seventy-five of the verified *Phragmites* points were randomly selected for use in the validation. A similar method was used to generate the *Not Phragmites* validation points. Two hundred points were randomly generated within the validation site, including the *Phragmites* patches. This allowed for points to be generated over non-*Phragmites* vegetation within or neighboring *Phragmites* patches. *Not Phragmites* points falling on a *Phragmites* plant were excluded from the validation set. One hundred points were randomly selected for the final *Not Phragmites* validation points. A total of 175 validation points were generated for the Chisago City property, the Swan Lake WMA, and the 2022 collection of the Wabasha property (Table 5). The amount of *Phragmites* present within the 2021 collection of the Chatfield WWTF and the 2022 collection of the Delano City Park limited the number of validation points. Thirty-five *Phragmites* validation points and 70 *Not Phragmites* validation points were selected for these two sites. A total of 105 validation points were used for these two collections (Table 5).

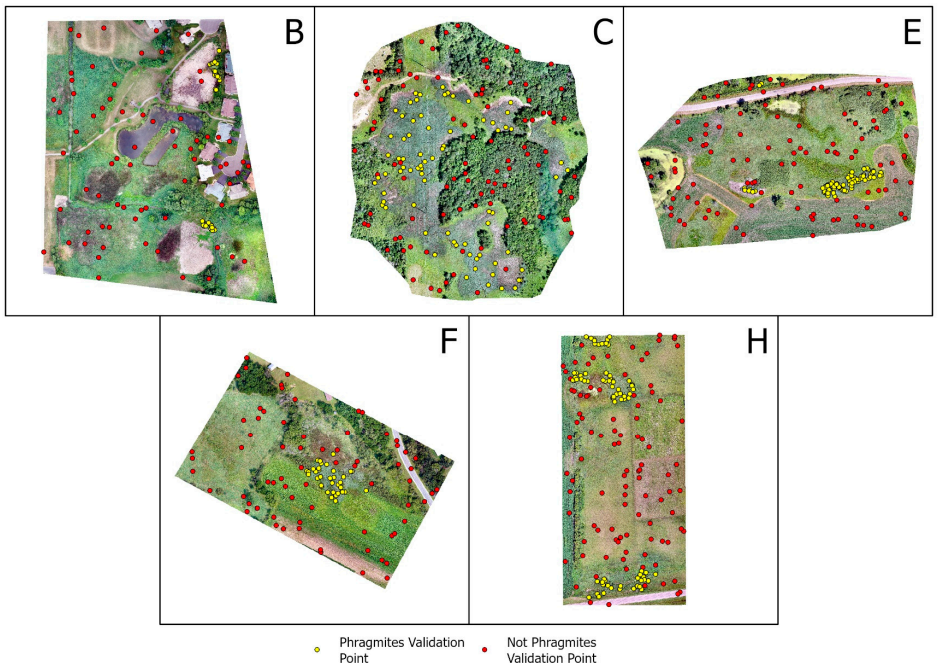


Figure 5. Location of validation points by cover class for the Delano City Park (**B**), Chisago City property (**C**), Wabasha property (2022) (**E**), Chatfield WWTF (2021) (**F**), and the Swan Lake WMA (**H**). Seventy-five *Phragmites* validation points and one hundred *Not Phragmites* validation points were randomly selected for the Chisago City property, Wabasha property (2022), and the Swan Lake WMA. Thirty-five *Phragmites* validation points and seventy *Not Phragmites* validation points were randomly selected for the Delano City Park and Chatfield WWTF (2021).

A confusion matrix was computed for each validation site by contrasting the predicted cover class at each validation point with the true cover class. Accuracy, including the producer's and user's accuracies, was calculated for each classification [72]. The validation points from the Chisago City property, Swan Lake WMA, and the 2022 collection of the Wabasha property were then merged. A combined confusion matrix from these three validation sites was created, and the combined overall, producer's, and user's accuracies

were reported. Validation points for the Delano City Park and the 2021 collection of the Chatfield WWTF were evaluated separately due to the lower number of validation points. Additionally, the Matthews Correlation Coefficient (MCC) was reported for each combined and individual classification. MCC determines a prediction's performance by comparing it to a random prediction [73], and it is a more reliable accuracy metric than the F1 score for binary classifications [74]. MCC ranges from negative one to one. A negative one corresponds to total disagreement, while a value of one corresponds to perfect prediction. An MCC value of zero suggests a classification that performed equally as well as a random guess. Accuracy was calculated for the following classifications: (1) MS classifier; (2) MS/CHM classifier without the post-ML OBIA rule set; (3) MS/CHM classifier with the post-ML OBIA rule set; (4) RGB classifier without the post-ML OBIA rule set; and (5) RGB classifier with the post-ML OBIA rule set. The post-ML OBIA rule set was not applied to the multispectral classification that did not include a CHM (MS classifier).

Table 5. Validation points per cover class for each validation collection. A total of 150 points were created for the *Phragmites* class, and 200 points were created for the Not *Phragmites* class. The number of verified points and the number randomly selected from the verified points are provided.

***Phragmites* Class**	**Generated**	**Verified**	**Selected**
Chisago City Property	150	98	75
Swan Lake WMA	150	88	75
Wabasha Property (2022)	150	88	75
Chatfield WWTF (2021)	150	43	35
Delano City Park	150	43	35
***Not Phragmites* Class**	**Generated**	**Verified**	**Selected**
Chisago City Property	200	151	100
Swan Lake WMA	200	191	100
Wabasha Property (2022)	200	196	100
Chatfield WWTF (2021)	200	194	70
Delano City Park	200	199	70

3. Results

3.1. Multispectral Classification

Each of the three validation sites was classified using the MS classifier, MS/CHM classifier without the post-ML OBIA rule set, and the MS/CHM classifier with the post-ML OBIA rule set (Figure 6). The MS classifier performed poorly, with classification accuracies ranging between 54–57% (Tables 6 and 7). A combined accuracy of 56% was attained. The combined user's accuracy for the *Phragmites* class was 30%, and the combined producer's accuracy was 3%. The *Not Phragmites* class performed better, with a combined user's accuracy of 57% and a combined producer's accuracy of 95%. Proper identification of *Phragmites* validation points was minimal across each of the three sites. No *Phragmites* validation points were correctly identified at either the Swan Lake WMA or the Wabasha property. The Chisago City property attained the highest user's and producer's accuracies for the *Phragmites* class with values of 43% and 8%, respectively. Computation of the user's accuracy for the *Phragmites* class at the Swan Lake WMA was impossible due to zero correctly identified *Phragmites* validation points and zero incorrectly identified *Not Phragmites* validation points. Identification of the *Not Phragmites* class was more successful than the *Phragmites* class across all three sites. Producer's accuracies for the *Not Phragmites* class ranged from 92–100%. The user's accuracies for the *Not Phragmites* class were lower, with values ranging between 56–57%. Poor classification accuracies were represented in the MCC estimates. The Chisago City property and the Swan Lake WMA both had MCC values of zero, and an MCC value of −0.16 was computed for the Wabasha property. A combined MCC value of −0.05 was achieved when using the MS classifier.

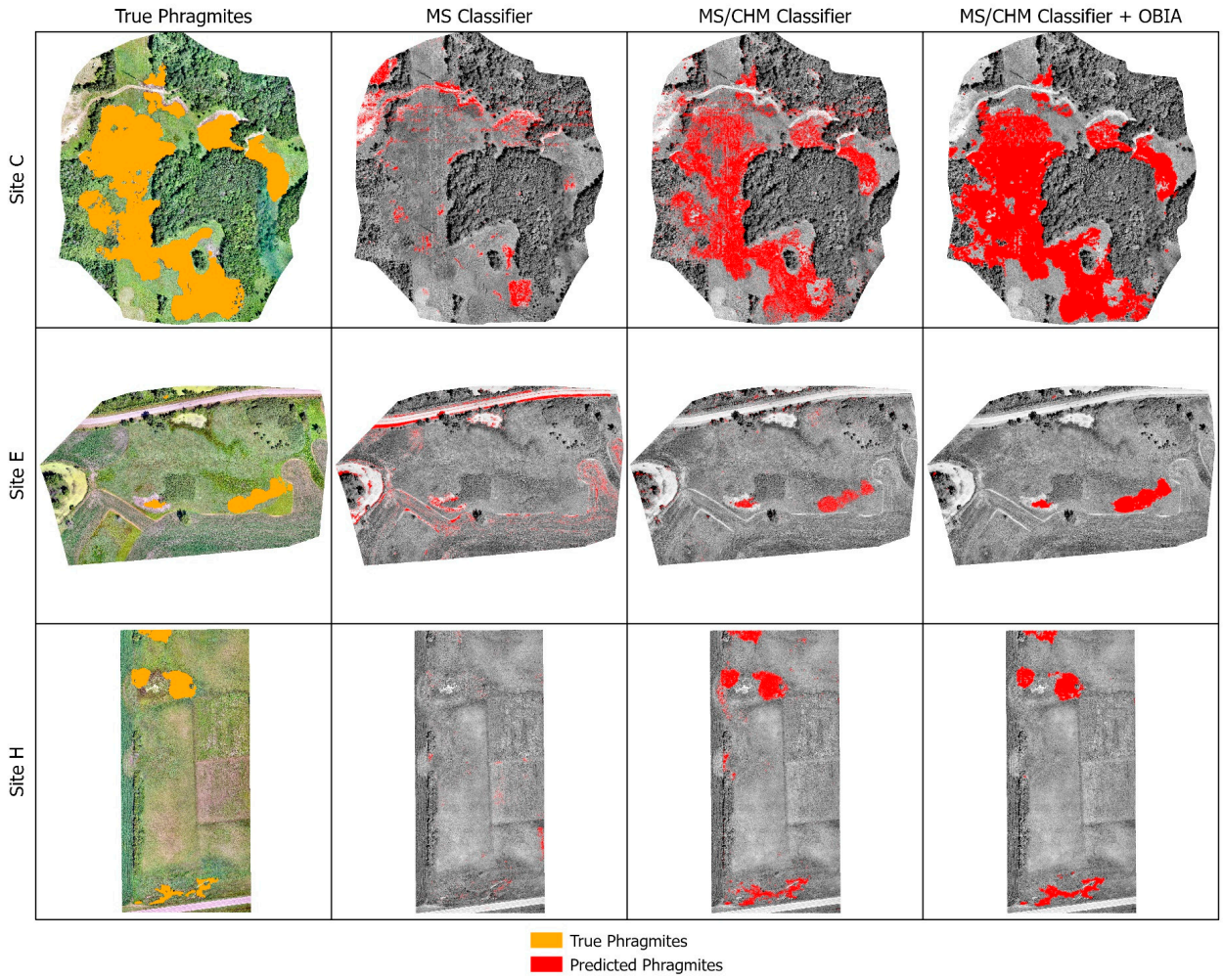


Figure 6. Classification of *Phragmites* (red) using the multispectral imagery without a canopy height model (MS Classifier), multispectral imagery with a canopy height model (MS/CHM Classifier), and the MS/CHM Classifier results after the application of the post-ML OBIA rule set (MS/CHM Classifier + OBIA) at the three validation sites: Chisago City property (**Site C**), Wabasha property (2022) (**Site E**), and the Swan Lake WMA (**Site H**). Everything not classified as *Phragmites* was predicted to be *Not Phragmites*. The true *Phragmites* location is provided as a reference (orange).

Table 6. Validation assessment points for each of the three validation sites for the multispectral ensemble classification without a canopy height model and a post-ML OBIA rule set.

	***Phragmites* Class**		***Not Phragmites* Class**	
Site	**Correct**	**Incorrect**	**Correct**	**Incorrect**
Chisago City Property	6	69	92	8
Swan Lake WMA	0	75	100	0
Wabasha Property	0	75	94	6
Combined	6	219	286	14

The inclusion of a CHM (MS/CHM classifier) improved the classification accuracy at each of the three validation sites. Combined overall accuracy increased to 81% (Tables 8 and 9). The combined producer's accuracy of the *Phragmites* class improved to 96%, and the combined user's accuracy improved to 58%. An increase in accuracy was also observed for the *Not Phragmites* class. A combined producer's accuracy of 98% and a user's accuracy of 76% was attained. The Swan Lake WMA experienced the largest increase in classification accuracy at the three validation sites. Accuracy for the Swan Lake WMA

increased from 57% to 83% with the addition of a CHM. The producer's accuracy for the *Phragmites* class increased from 0% to 57%, while the user's accuracy increased to 98%. The user's accuracy of the *Not Phragmites* class at the Swan Lake WMA improved to 75%, and the producer's accuracy decreased to 98%. Classification accuracy improved by 25% at both the Chisago City property and the Wabasha property. The *Phragmites* class at the Chisago City property attained a producer's accuracy of 57% and a user's accuracy of 96%. Similar values for the *Phragmites* class were calculated at the Wabasha property with a user's accuracy of 95% and a producer's accuracy of 55%. MCC values improved with the inclusion of a CHM. The Chisago City property achieved an MCC value of 0.63, Swan Lake WMA attained an MCC value of 0.68, and the Wabasha property achieved an MCC value of 0.61. An MCC value of 0.64 was calculated for the combined sites.

Table 7. User's Accuracy (UA), Producer's Accuracy (PA), Overall Accuracy (OA), and Matthews Correlation Coefficient (MCC) values for the multispectral ensemble classification without a canopy height model and a post-ML OBIA rule set.

Site	*Phragmites* Class		*Not Phragmites* Class		OA (%)	MCC
	UA (%)	PA (%)	UA (%)	PA (%)		
Chisago City Property	43	8	57	92	56	0
Swan Lake WMA	N/A	0	57	100	57	0
Wabasha Property	0	0	56	94	54	−0.16
Combined	30	3	57	95	56	−0.05

Table 8. Validation assessment points for the multispectral ensemble classification with a canopy height model but without a post-ML OBIA rule set.

Site	*Phragmites* Class		*Not Phragmites* Class	
	Correct	Incorrect	Correct	Incorrect
Chisago City Property	43	32	98	2
Swan Lake WMA	47	28	99	1
Wabasha Property	41	34	98	2
Combined	131	94	295	5

Table 9. User's Accuracy (UA), Producer's Accuracy (PA), Overall Accuracy (OA), and Matthews Correlation Coefficient (MCC) values for the multispectral ensemble classification with a canopy height model but without a post-ML OBIA rule set.

Site	*Phragmites* Class		*Not Phragmites* Class		OA (%)	MCC
	UA (%)	PA (%)	UA (%)	PA (%)		
Chisago City Property	96	57	75	98	81	0.63
Swan Lake WMA	98	57	75	98	83	0.68
Wabasha Property	95	55	74	98	79	0.61
Combined	96	58	76	98	81	0.64

The highest classification accuracies were achieved by the MS/CHM classifier with the post-ML OBIA rule set (Tables 10 and 11). A combined overall accuracy of 91% and an MCC value of 0.82 were attained. The combined user's accuracy for the *Phragmites* class was 95%, and it was 88% for the *Not Phragmites* class. The combined producer's accuracy for the *Phragmites* class was 83% and 97% for the *Not Phragmites* class. Classification accuracy improved the most at the Wabasha property. A user's accuracy of 100% was achieved by the *Phragmites* cover class as well as a producer's accuracy of 92%. The *Not Phragmites* class

attained a user's accuracy of 94% and a producer's accuracy of 100%. An overall accuracy of 97% was computed for the Wabasha property. The Swan Lake WMA showed the least improvement with the post-ML OBIA rule set. Overall accuracy at the Swan Lake WMA improved from 83% to 87%. Classification accuracy at the Chisago City property improved from 81% to 89%. Individual MCC values for each of the three sites ranged from 0.75–0.93.

Table 10. Validation assessment points for the multispectral ensemble classification with both a canopy height model and post-ML OBIA rule set.

	***Phragmites* Class**		***Not Phragmites* Class**	
Site	**Correct**	**Incorrect**	**Correct**	**Incorrect**
Chisago City Property	66	9	90	10
Swan Lake WMA	52	23	100	0
Wabasha Property	69	6	100	0
Combined	187	38	290	10

Table 11. User's Accuracy (UA), Producer's Accuracy (PA), Overall Accuracy (OA), and Matthews Correlation Coefficient (MCC) values for the multispectral ensemble classification with both a canopy height model and a post-ML OBIA rule set.

	***Phragmites* Class**		***Not Phragmites* Class**			
Site	**UA (%)**	**PA (%)**	**UA (%)**	**PA (%)**	**OA (%)**	**MCC**
Chisago City Property	87	88	91	90	89	0.78
Swan Lake WMA	100	69	81	100	87	0.75
Wabasha Property	100	92	94	100	97	0.93
Combined	95	83	88	97	91	0.82

Multispectral Classification of Withheld Validation Sites

Delano City Park and the Chatfield WWTF (2021 collection) were classified using the MS classifier, the MS/CHM classifier without the post-ML OBIA rule set, and the MS/CHM classifier with the post-ML OBIA rule set (Figure 7). The MS classifier resulted in the lowest classification accuracy at the Chatfield WWTF. An overall accuracy of 87% and an MCC value of 0.7 were achieved (Tables 12 and 13). A user's accuracy of 82% and a producer's accuracy of 77% were attained by the *Phragmites* class. The *Not Phragmites* class had a user's accuracy of 89% and a producer's accuracy of 91%. Classification accuracy increased with the MS/CHM classifier without the post-ML OBIA rule set. An overall accuracy of 94% and an MCC value of 0.87 were achieved. User's and producer's accuracies for the *Phragmites* class increased to 94% and 89%. The user's accuracy for the *Not Phragmites* class improved to 94%, but the producer's accuracy decreased to 89%. Overall accuracy decreased with the MS/CHM classifier with the post-ML OBIA rule set. An accuracy of 92% and an MCC value of 0.83 were achieved. The user's accuracy for the *Phragmites* class increased to 100%, while the producer's accuracy decreased to 77%. In contrast, the user's accuracy of the *Not Phragmites* class decreased to 90% while the producer's accuracy increased to 100%.

Classification of Delano City Park using the MS classifier resulted in an accuracy of 62%. Five of the thirty-five *Phragmites* validation points were correctly identified as *Phragmites*. This resulted in a user's accuracy of 50% and a producer's accuracy of 14% for the *Phragmites* class. Sixty of the seventy *Not Phragmites* validation points were correctly identified. This resulted in a user's accuracy of 67% and a producer's accuracy of 86%. Accuracy improved with the MS/CHM classifier without the post-ML OBIA rule set to 75%. Fifteen of the thirty-five *Phragmites* validation points were identified correctly, and sixty-four of the seventy *Not Phragmites* validation points were correctly identified. This resulted in a user's accuracy of 71% and a producer's accuracy of 43% for the *Phragmites* class. The *Not Phragmites* class attained a user's accuracy of 76% and a producer's accuracy of 91%.

Accuracy declined to 68% when including the post-ML OBIA rule set with the MS/CHM classifier. A single *Phragmites* point was correctly identified. As such, the *Phragmites* class achieved a user's accuracy of 100% and a producer's accuracy of 3%. A user's accuracy of 67% and a producer's accuracy of 100% were attained by the *Not Phragmites* class. MCC values for each of the three classifications followed a similar trend. An MCC value of zero was computed for the MS classifier, 0.4 for the MS/CHM classifier without the post-ML OBIA rule set, and 0.14 for the MS/CHM classifier with the post-ML OBIA rule set.

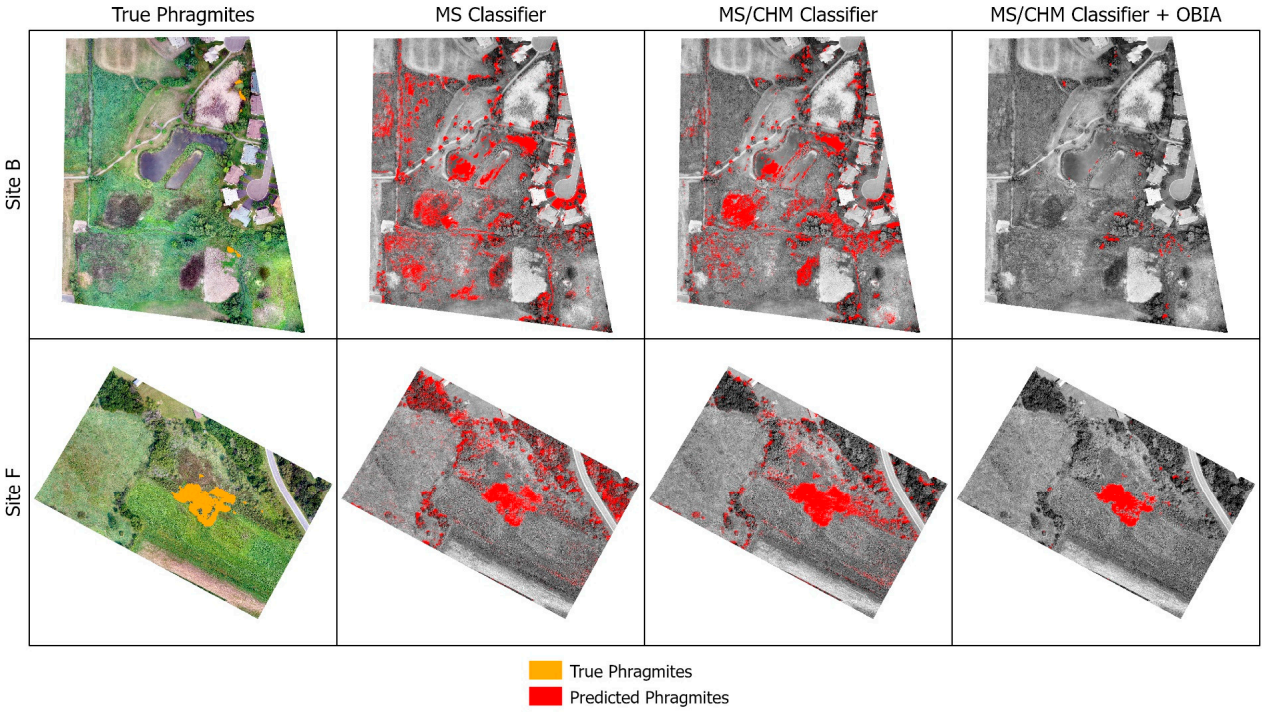


Figure 7. Classification of *Phragmites* (red) using the multispectral imagery without a canopy height model (MS Classifier), multispectral imagery with a canopy height model (MS/CHM Classifier), and the MS/CHM Classifier results after application of the post-ML OBIA rule set (MS/CHM Classifier + OBIA) at the two withheld validation sites: Delano City Park (**Site B**) and the Chatfield WWTF (2021) (**Site F**). Everything not classified as *Phragmites* was predicted to be *Not Phragmites*. The true *Phragmites* location is provided as a reference (orange).

Table 12. Validation assessment points for each of the three multispectral ensemble classifications at the two withheld validation sites: the 2021 Chatfield WWTF collection and the Delano City Park.

	***Phragmites* Class**		***Not Phragmites*Class**	
Delano City Park	**Correct**	**Incorrect**	**Correct**	**Incorrect**
MS	5	30	60	10
MS/CHM	15	20	64	6
MS/CHM + OBIA	1	34	70	0
Chatfield WWTF (2021)	**Correct**	**Incorrect**	**Correct**	**Incorrect**
MS	27	8	64	6
MS/CHM	31	4	68	2
MS/CHM + OBIA	27	8	70	0

Table 13. User's Accuracy (UA), Producer's Accuracy (PA), Overall Accuracy (OA), and Matthews Correlation Coefficient (MCC) values for the three multispectral ensemble classification at the two withheld validation sites: the 2021 Chatfield WWTF collection and the Delano City Park.

	***Phragmites*Class**		***NotPhragmites* Class**			
Delano City Park	**UA (%)**	**PA (%)**	**UA (%)**	**PA (%)**	**OA (%)**	**MCC**
MS	50	14	67	86	62	0
MS/CHM	71	43	76	91	75	0.4
MS/CHM + OBIA	100	3	67	100	68	0.14
Chatfield WWTF (2021)	**UA (%)**	**PA (%)**	**UA (%)**	**PA (%)**	**OA (%)**	**MCC**
MS	82	77	89	91	87	0.7
MS/CHM	94	89	94	89	94	0.87
MS/CHM + OBIA	100	77	90	100	92	0.83

3.2. RGB Classification

Each of the three validation sites was classified using the RGB classifier both with and without the post-ML OBIA rule set (Figure 8). The highest classification accuracy without the post-ML OBIA rule set was achieved at the Wabasha property (Tables 14 and 15). Sixty-eight of the seventy-five *Phragmites* validation points and ninety-seven of the one hundred *Not Phragmites* validation points were correctly identified. This resulted in an accuracy of 94% and an MCC value of 0.88. The *Phragmites* class achieved a user's accuracy of 96% and a producer's accuracy of 91%. User's and producer's accuracies for the *Not Phragmites* cover class were 93% and 97%. Accuracy and MCC values were lower at the Chisago City property. A user's accuracy of the *Phragmites* class was 88%. A producer's accuracy of the *Phragmites* class was 77%. The *Not Phragmites* class had high accuracies, with a user's accuracy of 84% and a producer's accuracy of 92%. Overall accuracy at the Chisago City property was 86%, with a computed MCC value of 0.71. Accuracy was lowest at the Swan Lake WMA. A user's accuracy of 87% and producer's accuracy of 53% were calculated for the *Phragmites* class. The *Not Phragmites* class achieved a user's accuracy of 73% and a producer's accuracy of 94%. Overall accuracy at the Swan Lake WMA was 77%, with an MCC value of 0.56. The combined classification accuracy of the RGB classifier without the post-ML OBIA rule set was 86%, with an MCC value of 0.74.

Minimal improvement was seen with the inclusion of the post-ML OBIA rule set (Tables 16 and 17). Overall accuracy at the Chisago City property increased by 1%, and the MCC value increased by 0.02. A user's accuracy for the *Phragmites* class improved to 90%, and the producer's accuracy increased to 80%. A slight improvement in the *Not Phragmites* class was recorded, with a user's accuracy of 86% and a producer's accuracy of 93%. The Swan Lake WMA had the largest increase in accuracy compared to the other two sites. Overall accuracy increased to 83%, and the MCC value improved to 0.67. The *Phragmites* class attained a user's accuracy of 94% and a producer's accuracy of 65%. A user's accuracy of 79% and a producer's accuracy of 97% were attained by the *Not Phragmites* class at the Swan Lake WMA. There were no changes in accuracy at the Wabasha property with the inclusion of the post-ML OBIA rule set.

Table 14. Validation assessment points for the RGB ensemble classification without the post-ML OBIA rule set.

	***Phragmites* Class**		***Not Phragmites* Class**	
Site	**Correct**	**Incorrect**	**Correct**	**Incorrect**
Chisago City Property	58	17	92	8
Swan Lake WMA	40	35	94	6
Wabasha Property	68	7	97	3
Combined	166	59	283	17

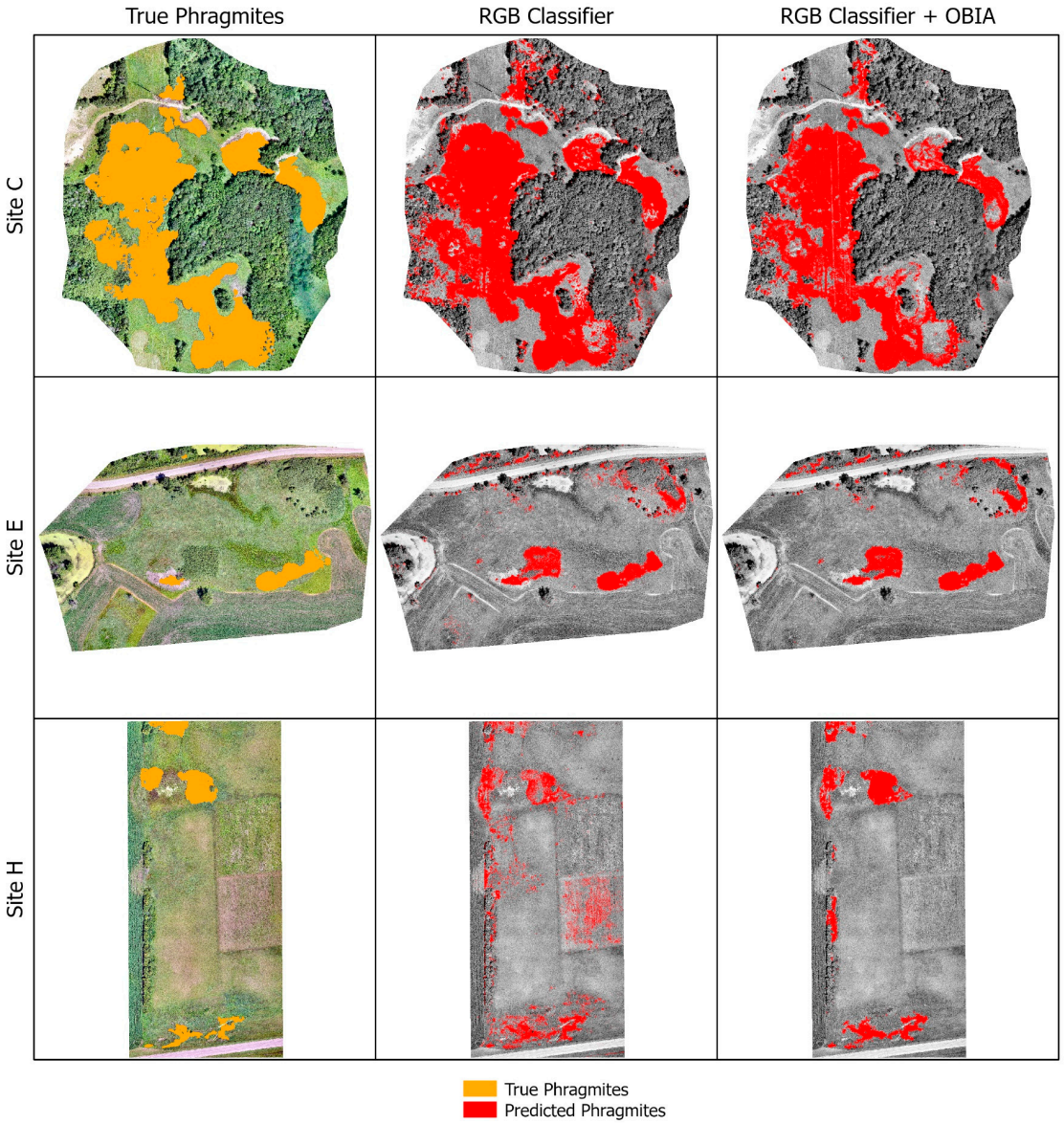


Figure 8. Classification of *Phragmites* (red) using the RGB imagery with a canopy height model (RGB Classifier) and the RGB Classifier results after application of the post-ML OBIA rule set (RGB Classifier + OBIA) at the three validation sites: Chisago City property (**Site C**), Wabasha property (2022) (**Site E**), and the Swan Lake WMA (**Site H**). Everything not classified as *Phragmites* was predicted to be *Not Phragmites*. The true *Phragmites* location is provided as a reference (orange).

Table 15. User's Accuracy (UA), Producer's Accuracy (PA), Overall Accuracy (OA), and Matthews Correlation Coefficient (MCC) values for the RGB ensemble classification without a post-ML OBIA rule set.

	***Phragmites* Class**		***Not Phragmites* Class**			
Site	**UA (%)**	**PA (%)**	**UA (%)**	**PA (%)**	**OA (%)**	**MCC**
Chisago City Property	88	77	84	92	86	0.71
Swan Lake WMA	87	53	73	94	77	0.56
Wabasha Property	96	91	93	97	94	0.88
Combined	91	80	86	94	86	0.74

Table 16. Validation assessment points for the RGB ensemble classification with the post-ML OBIA rule set.

	Phragmites Class		*Not Phragmites* Class	
Site	**Correct**	**Incorrect**	**Correct**	**Incorrect**
Chisago City Property	60	15	93	7
Swan Lake WMA	49	26	97	3
Wabasha Property	68	7	97	3
Combined	177	48	287	13

Table 17. User's Accuracy (UA), Producer's Accuracy (PA), Overall Accuracy (OA), and Matthews Correlation Coefficient (MCC) values for the RGB ensemble classification with the post-ML OBIA rule set.

	Phragmites Class		*Not Phragmites* Class			
Site	**UA (%)**	**PA (%)**	**UA (%)**	**PA (%)**	**OA (%)**	**MCC**
Chisago City Property	90	80	86	93	87	0.74
Swan Lake WMA	94	65	79	97	83	0.67
Wabasha Property	96	91	93	97	94	0.88
Combined	93	79	86	96	88	0.76

RGB Classification of Withheld Sites

The Delano City Park and the Chatfield WWTF (2021) were classified using the RGB classifier, both with and without the post-ML OBIA rule set (Figure 9). Twenty-eight of the thirty-five *Phragmites* validation points were correctly identified at the Delano City Park with the RGB classifier without the post-ML OBIA rule set (Table 18). Fifty-five of the seventy *Not Phragmites* points were correctly identified. This resulted in an overall accuracy of 79% and an MCC value of 0.56 (Table 19). The user's accuracy of the *Phragmites* class was 65%, and the producer's accuracy was 80%. The *Not Phragmites* class achieved a user's accuracy of 89% and a producer's accuracy of 79%. Overall accuracy at Delano City Park improved with the inclusion of the post-ML OBIA rule set, but fewer *Phragmites* validation points were identified correctly. A user's accuracy of 96% and a producer's accuracy of 69% were achieved by the *Phragmites* class with the inclusion of the post-ML OBIA rule set. Overall accuracy increased to 89% with an MCC value of 0.74. Calculated accuracy was the same for the RGB classifier both with and without the post-ML OBIA rule set at the Chatfield WWTF (2021 collection). User's and producer's accuracies for each class were above 90%. An overall accuracy of 97% and an MCC value of 0.94 were achieved.

Table 18. Validation assessment points for the RGB classifier both with and without the post-ML OBIA rule set at the two withheld validation sites: the 2021 Chatfield WWTF collection and the Delano City Park.

	Phragmites Class		*Not Phragmites* Class	
Delano City Park	**Correct**	**Incorrect**	**Correct**	**Incorrect**
RGB Classifier	28	7	55	15
RGB Classifier + OBIA	24	11	69	1
Chatfield WWTF (2021)	**Correct**	**Incorrect**	**Correct**	**Incorrect**
RGB Classifier	34	1	68	2
RGB Classifier + OBIA	34	1	68	2

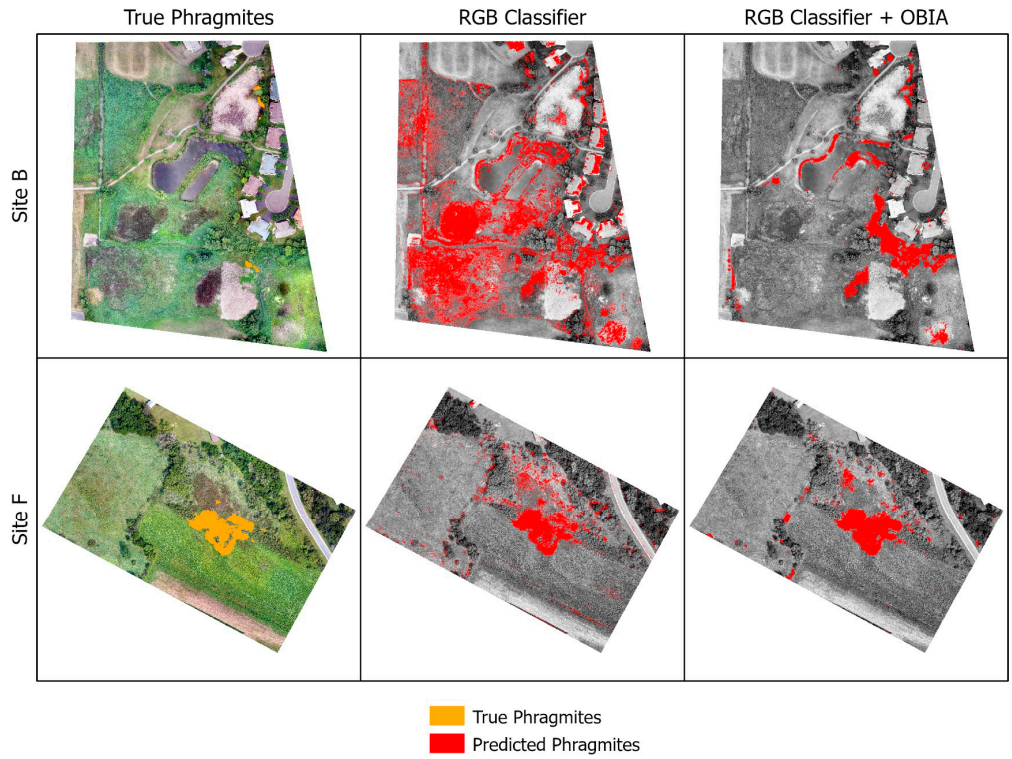


Figure 9. Classification of *Phragmites* (red) using the RGB imagery with a canopy height model (RGB Classifier) and the RGB Classifier results after application of the post-ML OBIA rule set (RGB Classifier + OBIA) at the two withheld validation sites: Delano City Park (**Site B**) and the Chatfield WWTF (2021) (**Site F**). Everything not classified as *Phragmites* was predicted to be *Not Phragmites*. The true *Phragmites* location is provided as a reference (orange).

Table 19. User's Accuracy (UA), Producer's Accuracy (PA), Overall Accuracy (OA), and Matthews Correlation Coefficient (MCC) values for the RGB classifier both with and without the post-ML OBIA rule set at the two withheld validation sites: the 2021 Chatfield WWTF collection and the Delano City Park.

	***Phragmites* Class**		***Not Phragmites* Class**			
Delano City Park	**UA (%)**	**PA (%)**	**UA (%)**	**PA (%)**	**OA (%)**	**MCC**
RGB Classifier	65	80	89	79	79	0.56
RGB Classifier + OBIA	96	69	86	99	89	0.74
Chatfield WWTF (2021)	**UA (%)**	**PA (%)**	**UA (%)**	**PA (%)**	**OA (%)**	**MCC**
RGB Classifier	94	97	99	97	97	0.94
RGB Classifier + OBIA	94	97	99	97	97	0.94

4. Discussion

4.1. Multispectral Classification

Accurate identification of *Phragmites* was not possible without the use of a CHM. A total of six *Phragmites* validation points were correctly identified across the three initial validation sites by the MS classifier. Classifications at the Swan Lake WMA and Chisago City property achieved MCC values of zero, which indicates that the classifications are no better than a random guess. *Phragmites* extent at each of the three initial validation sites was considerably underestimated. Significant portions of each site were classified as trees. Results using the MS classifier were consistent at Delano City Park, where five of the thirty-five *Phragmites* validation points were correctly identified. However, in contrast to the initial three validation sites, *Phragmites* extent was overestimated. This was consistent with the Chatfield WWTF, where a large number of trees and non-*Phragmites* herbaceous

vegetation were misidentified as *Phragmites*. Poor classification accuracies without a CHM were consistent with previous work [37]. Physical differentiation between *Phragmites* and non-*Phragmites* vegetation relies heavily on the height of *Phragmites* stems. Results from this study support conclusions from other studies that remote sensing classification techniques are unable to accurately identify *Phragmites* without a CHM. All applications using remote sensing for the automatic or semi-automatic detection of *Phragmites* should incorporate a CHM.

Classification accuracy improved with the addition of a CHM. A major issue with the MS classifier was the inability to differentiate trees from herbaceous vegetation. This was not as significant of an issue after the inclusion of a CHM. The voting-based ensemble classifier was able to properly distinguish trees from herbaceous vegetation. However, commission errors were present around the tree-herbaceous vegetation boundary. Some image objects at these boundaries contained small portions of the tree canopy, e.g., a few pixels. This would have skewed the distribution of heights within an image object, which may have led to misclassification. Issues around the tree-herbaceous vegetation boundary may be remedied through different multi-resolution segmentation parameters that better define the boundary of these vegetation types. Hierarchical image segmentation, as implemented in [54], would also provide a method for incorporating information on neighboring objects within a machine learning classifier. This could allow for better classification around the tree-herbaceous vegetation boundary by identifying neighboring objects that only contain tree canopy. Further sources of commission error were shorter trees, shrubs, and reed canary grass. Shorter trees and shrubs overlap in height with *Phragmites*. This resulted in misidentification at the Swan Lake WMA and Chisago City property. Misidentification of reed canary grass as *Phragmites* occurred when reed canary grass neighbored a *Phragmites* patch. It is possible that the image objects on the borders of the *Phragmites* patches were a mix of both *Phragmites* and reed canary grass. Incorporating imagery from multiple dates could be a potential solution to these commission errors. The appearance of many plants changes throughout the year. This study focused on identifying *Phragmites* from a single acquisition. The acquisition time selected in this study aimed to capture the maximum difference in height between *Phragmites* and neighboring wetland vegetation. It is possible that incorporating imagery from a different season may improve classification accuracy by capturing the seasonal differences in vegetation. This may be especially helpful for errors associated with deciduous trees and shrubs. Future research should examine whether the classification accuracy of *Phragmites* improves when using multiple dates of imagery.

Omission errors were also present with the MS/CHM classifier. *Phragmites* was less likely to be correctly identified at the periphery of a patch where stem density was lowest. This issue was present at the Swan Lake WMA, where the individual stems at the expanding edge of a *Phragmites* patch were not identified. The omission of image objects containing scattered *Phragmites* stems was likely due to the nature of the training data. The edges of *Phragmites* stands were excluded for training due to mixed vegetation at the periphery of patches. Errors omitting scattered *Phragmites* stems could possibly be remedied by adjusting training data to accommodate for *Phragmites* growing at lower stem densities. Image objects containing *Phragmites* were also omitted within a *Phragmites* patch. Portions of *Phragmites* patches were misclassified as shorter trees. This resulted in a fishnet pattern or pockets of omission within a *Phragmites* patch. The borders of *Phragmites* patches were not misidentified as shorter trees unless the patch bordered either larger trees, willows, or sumac. Overall, classification accuracy for the MS/CHM classifier at the three initial validation sites (81%) was lower than the 92.31% accuracy reported by Abeysinghe et al. (2019) [36], 91% reported by Samiappan et al. (2017) [35], 91.7% reported by Brooks et al. (2021) [62], 95% reported by Higgisson et al. (2021) [39], and the 95% accuracy reported by Guo et al. (2022) [75]. The producer's and user's accuracy for the *Phragmites* class were higher than those reported by Husson et al. (2016) [76].

Improved classification accuracy was achieved when applying the MS/CHM classifier to the two withheld validation sites. However, commission errors were more prevalent

compared to the three initial validation sites. Substantial error at the tree-herbaceous vegetation boundary was present at both the Delano City Park and the Chatfield WWTF. The number of commission errors was highest at Delano City Park where non-*Phragmites* herbaceous vegetation, such as cattails and reed canary grass, were commonly misidentified as *Phragmites*. Interestingly, sections of open water and mowed grass were also misidentified as *Phragmites*. Both of these cover types should be easily distinguishable from *Phragmites* within the CHM and NDVI image layers. Misidentification of open water as *Phragmites* was possibly due to not including an open water cover class during the training of the voting-based ensemble classifier. The Delano WWTF was the only training site to contain standing water, but the water was covered in duckweed (Lemnoidaea), making it unusable for training. The misclassification of open water could have been avoided by using the NDVI to remove image objects that do not contain vegetation before the voting-based ensemble classifier was applied. Misidentification of mowed grass was likely due to the proximity to trees or other tall surface features, such as houses. Similar to the tree-herbaceous vegetation boundary errors noted above, it is possible that these misidentified objects contained a mix of cover classes. Omission of low stem-density *Phragmites* was also present at the two withheld validation sites. Accuracy estimates for the two withheld sites varied. Delano City Park attained an accuracy similar to the three initial validation sites. Accuracy for the Chatfield WWTF was the highest among all validation sites at 94%.

The inclusion of the post-ML OBIA rule set resulted in the highest classification accuracies at the three initial validation sites. The post-ML OBIA rule set improved accuracy through the removal of commission errors and the filling of gaps within identified *Phragmites* patches. Combined classification accuracy (91%) was similar to those reported by others [35,36,41,62]. Results from the classification of the three initial validation sites support previous research that indicated improved accuracy with a post-ML OBIA rule set [41]. Errors were still present within the classifications despite the increase in accuracy. *Phragmites* patches at the Chisago City property were incorrectly expanded into neighboring non-*Phragmites* wetland vegetation due to the abundance of shrubs within the site. Image objects containing shrubs, whether a complete shrub canopy or a mix of shrub and herbaceous wetland vegetation, that neighbored *Phragmites* objects met the vegetation height requirement to be merged into *Phragmites* patches. This occurred on the western edge of the large *Phragmites* patch at the Chisago City property. The user's accuracy for the *Phragmites* class at the Chisago City property declined with the post-ML OBIA rule set as a result of the incorrect expansion. Commission errors were also present at the Wabasha property and Swan Lake WMA. *Phragmites* patches were incorrectly expanded into neighboring reed canary grass. Similar to the commission errors at the Chisago City property, this was the result of the Relative Border To rule merging image objects containing vegetation meeting a minimum height threshold. Omission errors, although greatly reduced, were still present in the final classification in the form of incorrect patch boundaries. Most of these errors occurred at the boundaries of *Phragmites* patches where stem densities were lowest. Image objects on the boundaries of *Phragmites* patches contained mixed vegetation. This resulted in the image objects not meeting the spectral or height thresholds needed to be reclassified as *Phragmites*. Most image objects containing scattered *Phragmites* stems on the periphery of a larger *Phragmites* patch were not initially classified as *Phragmites* by the voting-based ensemble classifier. However, it is likely that they would have been removed from the *Phragmites* class with the application of the post-ML OBIA rule set, even if they were correctly classified by the voting-based ensemble classifier. This is due to the small size of the image objects containing scattered *Phragmites* stems and due to the post-ML OBIA rule set not being tailored to identify *Phragmites* at lower stem densities. Minor changes could be made to the post-ML OBIA rule set to better accommodate for the lower stem densities seen at the expanding edges of a *Phragmites* patch. For example, the rule removing image objects from the *Phragmites* class if they do not meet a size threshold (in pixels) could be eliminated. Future work incorporating a post-ML OBIA rule set should

predetermine the accepted amount of commission and omission errors and build a rule set that meets project requirements.

Application of the post-ML OBIA rule set at the two withheld validation sites resulted in a reduction in classification accuracy. This was due to the omission of *Phragmites*. *Phragmites* was omitted for two reasons. First, small patches with low stem densities were wrongly removed. Second, the largest patch at the Chatfield WWTF is interspersed with shorter trees. The trees within the patch and their neighboring image objects were removed with the post-ML OBIA rule set. Image objects containing *Phragmites* were removed due to them bordering tree objects. Commission errors were significantly reduced at the Chatfield WWTF despite the increase in omission errors. A large number of image objects situated at the tree-herbaceous vegetation boundary were misclassified as *Phragmites* without the post-ML OBIA rule set. Few of these misclassified image objects remained after the application of the post-ML OBIA rule set. Accuracy at the Chatfield WWTF was similar to those achieved at the three initial validation sites and those attained by others [35,36,41,62]. Application of the post-ML OBIA rule set at Delano City Park resulted in the failure of the classifier. All of the *Phragmites* present at Delano City Park has a low stem density due to prior chemical treatment. Image objects containing scattered *Phragmites* stems were removed due to the design of the OBIA rule set. This resulted in the correct identification of fourteen fewer *Phragmites* validation points compared to the classification without the post-ML OBIA rule set. The accuracy and MCC value at Delano City Park were slightly higher than the classification without the CHM due to the removal of commission errors. Results at Delano City Park further demonstrate the inability of the post-ML OBIA rule set used in this study to properly identify *Phragmites* at lower stem densities.

4.2. RGB Classification

The RGB classifier outperformed the MS/CHM classifier at the three initial validation sites when not using the post-ML OBIA rule set. Visual analysis of the classifications indicated that the RGB classifier performed best at the Chisago City property. Similar commission errors occurred around the tree-herbaceous vegetation boundary. The interior of the large *Phragmites* patches was well-defined compared to the results from the MS/CHM classifier that produced a fishnet-like pattern. The omission of *Phragmites* occurred in areas with lower stem densities. Despite the increase in accuracy, visual analysis of the RGB classifications indicated that the RGB classifier did not outperform the MS/CHM classifier at the Wabasha property and the Swan Lake WMA. A significant number of willows at the center of the Wabasha property were misclassified as *Phragmites*. Comparatively, the MS/CHM classifier was able to classify these trees correctly. Misclassification of non-*Phragmites* vegetation at the tree-herbaceous vegetation border was widespread at both the Wabasha property and Swan Lake WMA. Further misclassification of herbaceous, non-*Phragmites* vegetation was abundant at the Swan Lake WMA. Reed canary grass adjacent to the southernmost *Phragmites* patch and upland grass on the eastern side of the site were falsely classified as *Phragmites*. The omission of *Phragmites* was minimal at the Wabasha property. The greater omission occurred at the Swan Lake WMA, where portions of each native *Phragmites* patch were incorrectly classified as *Short Tree*. Classification accuracy of the three initial validation sites (86%) was similar to those reported in Anderson et al. (2023) without the use of a post-ML OBIA rule set [41] and lower than those published by others [35,36,39,62]. Results at the two withheld validation sites varied. The RGB classifier failed to accurately distinguish *Phragmites* from non-*Phragmites* cover types at Delano City Park. Cattails and reed canary grass were consistently misidentified as *Phragmites*. Due to the amount of commission error at Delano City Park, it is unclear whether the *Phragmites* was intentionally identified or if the *Phragmites* was identified by chance. The RGB classifier without the post-ML OBIA rule set attained the highest accuracy at the Chatfield WWTF. All *Phragmites* was correctly identified except for the omission of scattered stems. Commission errors were present at the tree-herbaceous vegetation boundary, which was consistent with results at other validation sites with the RGB classifier and MS/CHM classifier. The

accuracy attained at the Chatfield WWTF was higher than the 94% reported by Higgisson et al. (2021) [39] and the 95% published by Guo et al. (2022) [75].

Application of the post-ML OBIA rule set from [41] resulted in a negligible increase in classification accuracy. The omission of *Phragmites* on the interior of large patches was minimal with the RGB classifier compared to the MS/CHM classifier before the application of the post-ML OBIA rule set. This resulted in a smaller increase in classification accuracy for the RGB classifier once the post-ML OBIA rule set was applied. The omission of *Phragmites* after the application of the post-ML OBIA rule set mostly occurred in areas of low stem densities. Commission errors were reduced at the Chisago City property, but the validation points did not capture this change. No change in accuracy was recorded at the Wabasha property. The largest change in classification accuracy was observed at the Swan Lake WMA. A significant amount of the misclassified reed canary grass, upland grass, and vegetation at the tree-herbaceous vegetation boundary was removed from the *Phragmites* cover class. Gaps within the three northern *Phragmites* patches were filled or lessened. Mixed results were observed at the two withheld validation sites. Increased accuracy at Delano City Park was the result of reducing commission errors. Significant areas of misidentified, non-*Phragmites* vegetation were removed from the *Phragmites* class. Fewer *Phragmites* validation points were correctly identified at Delano City Park with the application of the post-ML OBIA rule set. This was due to the removal of image objects containing small, scattered *Phragmites* stems. No changes in classification accuracy were calculated at the Chatfield WWTF despite a reduction in commission errors and the omission of one *Phragmites* patch. Despite the minimal change in classification accuracy, visual analysis of the classifications post-processed with the post-ML OBIA rule set shows an improvement compared to classifications without the post-ML OBIA rule set.

4.3. Which Methods Should Be Used for Phragmites Detection?

Selecting methodology can be a difficult decision for resource managers who have chosen to use UAS for *Phragmites* surveillance. Choices need to be made regarding the vehicle, sensor, classification techniques, etc. This research provides insight into two aspects: sensors and classification techniques. Results from this study suggest that multispectral imagery should be used to identify *Phragmites* when possible (Figure 10). This remains true without the use of the post-ML OBIA rule set. The fishnet pattern observed with the MS/CHM classifier misclassifying image objects on the interior of *Phragmites* patches resulted in a lower accuracy compared to the RGB classifier. However, it is recommended to use multispectral imagery despite the omission of the interior of *Phragmites* patches. This is because the commission errors with the MS/CHM classifier were significantly less than the RGB classifier when compared visually. The use of RGB imagery would still be sufficient if multispectral imagery is unavailable as the RGB classifier accurately captured the interior of *Phragmites* patches. The most critical component for the accurate classification of *Phragmites* is a CHM. This study created digital surface models from the RGB imagery. The multispectral sensor used in this study captured images with a lower spatial resolution compared to the RGB sensor, and the multispectral sensor was unable to integrate with the post-processing kinematic capabilities of the Microdrones MD4-1000. Creation of surface models from the multispectral imagery would have required the placement of additional ground control points at the study sites or the co-registration of the created surface models to the lidar data to ensure alignment. Placement of ground control points can be complicated if survey locations are physically inaccessible. It was determined to be more appropriate to use the surface models derived from the RGB imagery in our study due to the higher spatial resolution and multiple sites with too few ground control points. However, it is possible to substitute the RGB imagery with the multispectral imagery for the creation of surface models. Multispectral sensors and processing pipelines exist that can produce point clouds as accurately as point clouds derived from RGB imagery [77]. Care should be taken before the purchase of a multispectral sensor to ensure that the sensor has the specifications required to produce accurate surface models, e.g., focal length and

autofocus and post-processing or real-time kinematic integration [78]. Post-processing or real-time kinematics may not be necessary if survey locations allow for the placement of a suitable amount of ground control points. Similar data acquisition methods used in this study can also be implemented effectively at the cost of two flights per target area (RGB and multispectral).

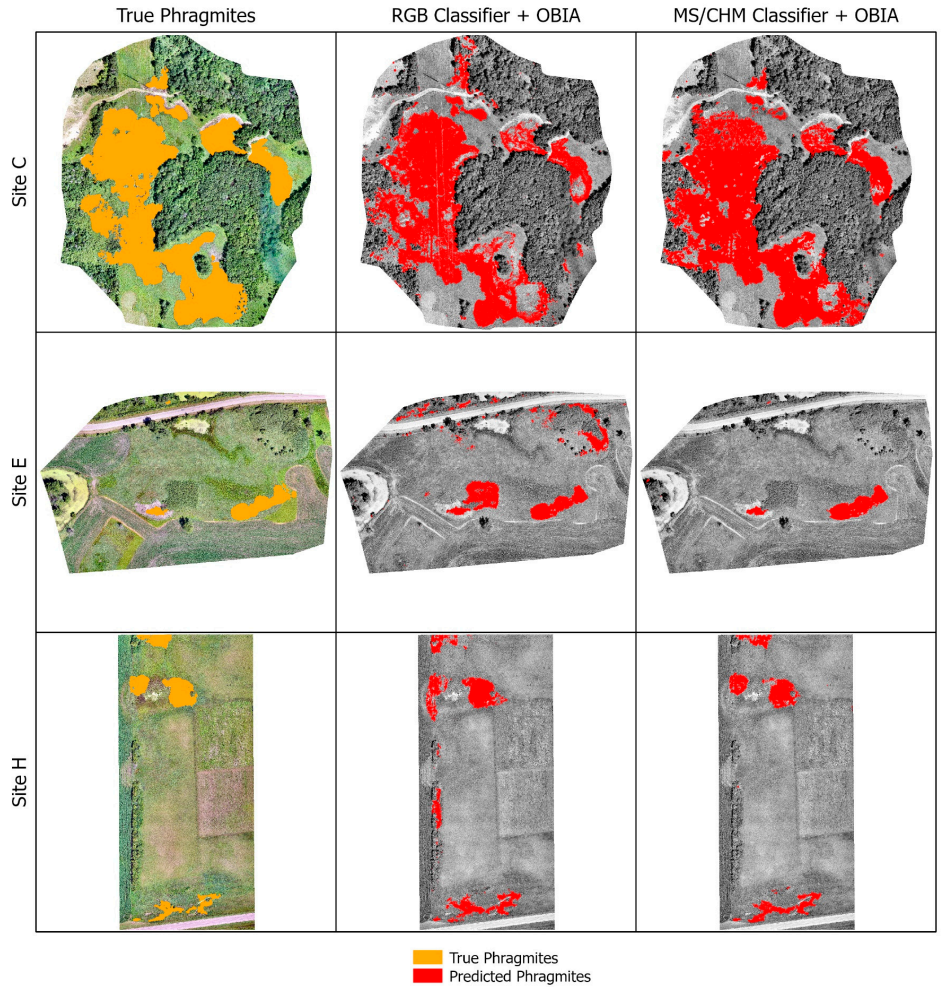


Figure 10. Classification of *Phragmites* (red) using the RGB classifier with the post-ML OBIA rule set and the MS/CHM classifier with the post-ML OBIA rule set at the three validation sites: Chisago City Property (**Site C**), Wabasha property (**Site E**), and the Swan Lake Wildlife Management Area (**Site H**). Everything not identified as *Phragmites* was classified as *Not Phragmites*. The true *Phragmites* location is provided as a reference (orange).

Numerous classification methods have been applied to detect *Phragmites* from UAS imagery, including manual image interpretation [33,76], pixel-based classification using an SVM [35,36,40,55], ANN [36,40], Maximum Likelihood Classifier [40], RF [55], object-based classifications using an OBIA rule set [37], the nearest neighbor algorithm [36,62], SVM [36,41,55], RF [41,55,76], ANN [36,41], and classifications of *Phragmites* with convolutional neural networks [38,39,75]. A majority of the studies implementing these aforementioned methods have reported accuracies higher than 90%, including this study. Resource managers applying UAS for *Phragmites* detection will likely rely on a machine learning algorithm to classify their imagery. Deciding which machine learning algorithm to use is a challenging decision due to the similar results with multiple classification techniques. Results from this study suggest that *Phragmites* can be accurately mapped using voting-based ensemble classifiers containing different machine learning algorithms. The methods used in this study provide a pathway to avoid a decision on a single machine learning algorithm.

Voting-based ensemble classifiers can also account for the variability between classifications from different machine learning algorithms by combining the predictions through hard or soft voting criteria. We suggest that resource specialists managing *Phragmites* use a voting-based ensemble classifier for future detection of *Phragmites* from UAS imagery, but we do not name specific machine learning algorithms to be included. Results from other studies indicate that most machine learning algorithms are capable of identifying *Phragmites* with high accuracy. It is possible that no "best" algorithm exists for *Phragmites* identification or that the "best" algorithm changes between sites or times. The "best" algorithm may also change due to data pre-processing techniques, classification goals (e.g., single *Phragmites* stems, live versus dead *Phragmites*, etc.), pixel-based versus object-based classifications, and a user's familiarity with different machine learning algorithms. We recommend selecting several machine learning algorithms users are most familiar with. Further research is needed to determine the optimal number of distinct machine learning classifiers within a voting-based ensemble framework to ensure the transferability of a classifier to new wetlands.

Results from this study support those from Anderson et al. (2023) [41] that indicate the ability of a post-ML OBIA rule set to improve machine learning classification accuracies of *Phragmites*. It is suggested that machine learning classifications of *Phragmites* be paired with OBIA post-processing techniques, such as those demonstrated here. A general concern with object-based rule sets is their transferability to new locations. The improved classification accuracy calculated at multiple validation sites with the application of a post-ML OBIA rule set for both this study and [41] indicates that transferability may be possible to new wetlands across Minnesota as long as they contain similar vegetation types and structures. This was possible because the rule sets used herein were not the basis from which *Phragmites* was identified. They instead focused on improving an existing classification using contextual-based rules, and the *Phragmites* grew similarly across all validation sites. We suggest that future work using OBIA to post-process machine learning classifications of *Phragmites* follow a similar context-based framework. Despite their generalized design, it is unlikely that the post-ML OBIA rule sets used in this study would succeed in all wetland types within Minnesota. However, it is also unlikely that a machine learning algorithm would succeed across multiple wetland types due to the change in non-*Phragmites* vegetation, as was noted by Anderson et al. (2023) [41]. Resource specialists managing for Phragmites should not apply these methods to areas substantially different than their training sites. Additional research is needed to determine the extent to which OBIA post-processing of machine learning classifications of *Phragmites* can scale to new sites.

5. Conclusions

UAS are useful for detecting and monitoring invasive *Phragmites* due to the high spatial resolution, high temporal resolution, and the ability to compute surface models from the acquired images. Semi-automated or automated prediction of *Phragmites* extent within UAS imagery using machine learning can be challenging since it is not always possible to have the a priori knowledge on which specific machine learning algorithm will produce the most accurate results. This study examined a voting-based ensemble classifier for its ability to identify *Phragmites* within five Minnesota wetlands from both RGB UAS imagery and multispectral UAS imagery. Results from this research suggest that a voting-based ensemble classifier can be used to accurately map established *Phragmites* patches from both RGB and multispectral UAS imagery. This was demonstrated by achieving classification accuracies greater than 80% without the post-ML OBIA rule set and accuracies greater than or equal to 88% with the post-ML OBIA rule set. Predictions using the multispectral UAS imagery were especially accurate due to the minimal misclassification of non-*Phragmites* vegetation. However, the techniques used in this study failed to accurately identify *Phragmites* at lower stem densities despite their high overall accuracy. This issue was especially apparent at Delano City Park, where the most accurate classifier at the three initial validation sites

(MS/CHM + OBIA) failed to identify all but one *Phragmites* validation point. Failure to identify sparse *Phragmites* raises concerns about the applicability of UAS to identify new populations, which tend to have lower stem densities than established source populations. Image classification techniques trained on dense *Phragmites* patches may unknowingly omit the *Phragmites* patches with low stem densities generally associated with the expanding front of the invasion. Future work should explore image classification techniques for the accurate identification of individual *Phragmites* stems or patches with low stem density. The ability to detect the expanding front of the *Phragmites* invasion is critical if resource specialists coordinating *Phragmites* management are to use UAS for *Phragmites* surveillance.

Author Contributions: Conceptualization, C.J.A. and J.F.K.; data curation, C.J.A. and D.H.; methodology, C.J.A., D.H., K.C.P. and J.F.K.; formal analysis, C.J.A.; validation, C.J.A.; writing—original draft preparation, C.J.A.; writing—review and editing, C.J.A., D.H., K.C.P. and J.F.K.; funding acquisition, J.F.K. All authors have read and agreed to the published version of the manuscript.

Funding: This work was funded by the Legislative and Citizen Commission for Minnesota Resources through Minnesota's Environment and Natural Resources Trust Fund (ENRTF) via the Minnesota Invasive Terrestrial Plant and Pest Center (MITPPC) grant number ML2018 Ch214 Art.4 Sec.2 Sub.06a E818ITP.

Data Availability Statement: No new data were created in this study. Data sharing is not applicable to this article.

Conflicts of Interest: The authors declare no conflict of interest.

References

1. Adhikari, S.; Bajracharaya, R.M.; Sitaula, B.K. A Review of Carbon Dynamics and Sequestration in Wetlands. *J. Wetl. Ecol.* **2009**, *2*, 42–46. [CrossRef]
2. Costanza, R.; D'Arge, R.; de Groot, R.; Farber, S.; Grasso, M.; Hannon, B.; Limburg, K.; Naeem, S.; O'Neill, R.V.; Paruelo, J.; et al. The value of the world's ecosystem services and natural capital. *Nature* **1997**, *387*, 253–260. [CrossRef]
3. Davidson, N.C. How much wetland has the world lost? Long-term and recent trends in global wetland area. *Mar. Freshw. Res.* **2014**, *65*, 934–941. [CrossRef]
4. Hu, S.; Niu, Z.; Chen, Y.; Li, L.; Zhang, H. Global wetlands: Potential distribution, wetland loss, and status. *Sci. Total Environ.* **2017**, *586*, 319–327. [CrossRef]
5. Dahl, T.E. *Wetlands Losses in the United States 1780's to 1980's*; United States Department of the Interior, Fish and Wildlife Service: Washington, DC, USA, 1990.
6. Gallardo, B.; Clavero, M.; Sánchez, M.I.; Vilà, M. Global ecological impacts of invasive species in aquatic ecosystems. *Glob. Chang. Biol.* **2016**, *22*, 151–163. [CrossRef]
7. Templer, P.; Findlay, S.; Wigand, C. Sediment chemistry associated with native and non-native emergent macrophytes of a hudson river marsh ecosystem. *Wetlands* **1998**, *18*, 70–78. [CrossRef]
8. Windham, L.; Meyerson, L.A. Effects of Common Reed (*Phragmites australis*) Expansions on Nitrogen Dynamics of Tidal Marshes of the Northeastern U.S. *Estuaries* **2003**, *26*, 452–464. [CrossRef]
9. Vilà, M.; Espinar, J.L.; Hejda, M.; Hulme, P.E.; Jarošík, V.; Maron, J.L.; Pergl, J.; Schaffner, U.; Sun, Y.; Pyšek, P. Ecological impacts of invasive alien plants a meta-analysis of their effects on species. *Ecol. Lett.* **2011**, *14*, 702–708. [CrossRef]
10. Olson, D.H.; Aanensen, D.M.; Ronnenberg, K.L.; Powell, C.I.; Walker, S.F.; Bielby, J.; Garner, T.W.J.; Weaver, G.; Fisher, M.C. Mapping the Global Emergence of *Batrachochytrium dendrobatidis*, the Amphibian Chytrid Fungus. *PLoS ONE* **2013**, *8*, e56802. [CrossRef]
11. Pimentel, D.; Zuniga, R.; Morrison, D. Update on the environmental and economic costs associated with alien-invasive species in the United States. *Ecol. Econ.* **2005**, *52*, 273–288. [CrossRef]
12. Morais, P.; Reichard, M. Cryptic invasions: A review. *Sci. Total Environ.* **2018**, *613*, 1438–1448. [CrossRef]
13. Saltonstall, K. Cryptic invasion by a non-native genotype of the common reed, *Phragmites australis*, into North America. *Proc. Natl. Acad. Sci. USA* **2002**, *99*, 2445–2449. [CrossRef] [PubMed]
14. Minnesota Department of Agriculture. 2022 Noxious Weed List. 2022. Available online: https://www.mda.state.mn.us/sites/default/files/docs/2022-02/2022NoxiousWeedListFactsheet.pdf (accessed on 1 January 2023).
15. Saltonstall, K.; Burdick, D.; Miller, S.; Smith, B. *Native and Non-Native Phragmites: Challenges in Identification, Research, and Management of the Common Reed*; National Estuarine Research Reserve: Washington, DC, USA, 2005.
16. Galatowitsch, S.M.; Anderson, N.O.; Ascher, P.D. Invasiveness in Wetland Plants in Temperate North America. *Wetlands* **1999**, *19*, 733–755. [CrossRef]
17. Chambers, R.M.; Osgood, D.T.; Bart, D.J.; Montalato, F. *Phragmites australis* Invasion and Expansion in Tidal Interactions among Salinity, Sulfide, and Hydrology. *Estuaries* **2003**, *26*, 398–406. [CrossRef]

18. Hocking, P.J.; Finlayson, C.M.; Chick, A.J. The biology of Australian weeds. 12. *Phragmites australis (Cav.) Trin. Ex Steud. J. Aust. Inst. Agric. Sci.* **1983**, *49*, 123–132.
19. Bernal, B.; Megonigal, J.P.; Mozdzer, T.J. An invasive wetland grass primes deep soil carbon pools. *Glob. Chang. Biol.* **2017**, *23*, 2104–2116. [CrossRef]
20. Findlay, S.E.G.; Dye, S.; Kuehn, K.A. Microbial Growth and Nitrogen Retention in Litter of *Phragmites australis* Compared To Typha Angustifolia, Wetlands. *Wetlands* **2002**, *22*, 616–625. [CrossRef]
21. Meyerson, L.A.; Saltonstall, K.; Windham, L.; Kiviat, E.; Findlay, S. A comparison of *Phragmites australis* in freshwater and brackish marsh environments in North America. *Wetl. Ecol. Manag.* **2000**, *8*, 89–103. [CrossRef]
22. Weinstein, M.P.; Balletro, J.H. Does the Common Reed, *Phragmites australis*, Affect Essential Fish Habitat. *Estuaries* **1999**, *22*, 793–802. [CrossRef]
23. Chambers, R.M.; Meyerson, L.A.; Saltonstall, K. Expansion of *Phragmites australis* into tidal wetlands of North America. *Aquat. Bot.* **1999**, *64*, 261–273. [CrossRef]
24. Marks, M.; Lapin, B.; Randall, J. *Phragmites australis* (*P. communis*): Threats, Management, and Monitoring. *Source Nat. Areas J.* **1994**, *14*, 285–294.
25. EDDMapS. Early Detection and Distribution Mapping System. Available online: https://www.eddmaps.org/ (accessed on 23 March 2023).
26. Pengra, B.W.; Johnston, C.A.; Loveland, T.R. Mapping an invasive plant, *Phragmites australis*, in coastal wetlands using the EO-1 Hyperion hyperspectral sensor. *Remote Sens. Environ.* **2007**, *108*, 74–81. [CrossRef]
27. Ghioca-Robrecht, D.M.; Johnston, C.A.; Tulbure, M.G. Assessing the use of multiseason quickbird imagery for mapping invasive species in a Lake Erie coastal marsh. *Wetlands* **2008**, *28*, 1028–1039. [CrossRef]
28. Laba, M.; Downs, R.; Smith, S.; Welsh, S.; Neider, C.; White, S.; Richmond, M.; Philpot, W.; Baveye, P. Mapping invasive wetland plants in the Hudson River National Estuarine Research Reserve using quickbird satellite imagery. *Remote Sens. Environ.* **2008**, *112*, 286–300. [CrossRef]
29. Bourgeau-Chavez, L.L.; Kowalski, K.P.; Carlson Mazur, M.L.; Scarbrough, K.A.; Powell, R.B.; Brooks, C.N.; Huberty, B.; Jenkins, L.K.; Banda, E.C.; Galbraith, D.M.; et al. Mapping invasive *Phragmites australis* in the coastal Great Lakes with ALOS PALSAR satellite imagery for decision support. *J. Great Lakes Res.* **2013**, *39*, 65–77. [CrossRef]
30. Rupasinghe, P.A.; Chow-Fraser, P. Mapping Phragmites cover using WorldView 2/3 and Sentinel 2 images at Lake Erie Wetlands, Canada. *Biol. Invasions* **2021**, *23*, 1231–1247. [CrossRef]
31. Müllerová, J.; Pergl, J.; Pyšek, P. Remote sensing as a tool for monitoring plant invasions: Testing the effects of data resolution and image classification approach on the detection of a model plant species *Heracleum mantegazzianum* (giant hogweed). *Int. J. Appl. Earth Obs. Geoinf.* **2013**, *25*, 55–65. [CrossRef]
32. Müllerová, J.; Brůna, J.; Dvořák, P.; Bartaloš, T.; Vítková, M. Does the data resolution/origin matter? Satellite, airborne and UAV imagery to tackle plant invasions. *Int. Arch. Photogramm. Remote Sens. Spat. Inf. Sci. ISPRS Arch.* **2016**, *41*, 903–908. [CrossRef]
33. Husson, E.; Hagner, O.; Ecke, F. Unmanned aircraft systems help to map aquatic vegetation. *Appl. Veg. Sci.* **2014**, *17*, 567–577. [CrossRef]
34. Samiappan, S.; Turnage, G.; Hathcock, L.; Casagrande, L.; Stinson, P.; Moorhead, R. Using unmanned aerial vehicles for high-resolution remote sensing to map invasive *Phragmites australis* in coastal wetlands. *Int. J. Remote Sens.* **2016**, *38*, 2199–2217. [CrossRef]
35. Samiappan, S.; Turnage, G.; Hathcock, L.A.; Moorhead, R. Mapping of invasive phragmites (common reed) in Gulf of Mexico coastal wetlands using multispectral imagery and small unmanned aerial systems. *Int. J. Remote Sens.* **2017**, *38*, 2861–2882. [CrossRef]
36. Abeysinghe, T.; Milas, A.S.; Arend, K.; Hohman, B.; Reil, P.; Gregory, A.; Vázquez-Ortega, A. Mapping invasive *Phragmites australis* in the Old Woman Creek estuary using UAV remote sensing and machine learning classifiers. *Remote Sens.* **2019**, *11*, 1380. [CrossRef]
37. Anderson, C.J.; Heins, D.; Pelletier, K.C.; Bohnen, J.L.; Knight, J.F. Mapping Invasive *Phragmites australis* Using Unoccupied Aircraft System Imagery, Canopy Height Models, and Synthetic Aperture Radar. *Remote Sens.* **2021**, *13*, 3303. [CrossRef]
38. Cohen, J.G.; Lewis, M.J. Development of an Automated Monitoring Platform for Invasive Plants in a Rare Great Lakes Ecosystem Using Uncrewed Aerial Systems and Convolutional Neural Networks. In Proceedings of the 2020 International Conference on Unmanned Aircraft Systems, ICUAS 2020, Athens, Greece, 1–4 September 2020; pp. 1553–1564.
39. Higgisson, W.; Cobb, A.; Tschierschke, A.; Dyer, F. Estimating the cover of *Phragmites australis* using unmanned aerial vehicles and neural networks in a semi-arid wetland. *River Res. Appl.* **2021**, *37*, 1312–1322. [CrossRef]
40. Mohler, R.L.; Morse, J.M. Using UAV imagery to map invasive *Phragmites australis* on the Crow Island State Game Area, Michigan, USA. *Wetl. Ecol. Manag.* **2022**, *30*, 1213–1229. [CrossRef]
41. Anderson, C.J.; Heins, D.; Pelletier, K.C.; Knight, J.F. Improving Machine Learning Classifications of *Phragmites australis* Using Object-Based Image Analysis. *Remote Sens.* **2023**, *15*, 989. [CrossRef]
42. Sachdeva, S.; Bhatia, T.; Verma, A.K. A novel voting ensemble model for spatial prediction of landslides using GIS. *Int. J. Remote Sens.* **2020**, *41*, 929–952. [CrossRef]
43. Aguilar, R.; Zurita-Milla, R.; Izquierdo-Verdiguier, E.; de By, R.A. A cloud-based multi-temporal ensemble classifier to map smallholder farming systems. *Remote Sens.* **2018**, *10*, 729. [CrossRef]

44. Foody, G.M.; Boyd, D.S.; Sanchez-Hernandez, C. Mapping a specific class with an ensemble of classifiers. *Int. J. Remote Sens.* **2007**, *28*, 1733–1746. [CrossRef]
45. Liu, X.; Liu, H.; Datta, P.; Frey, J.; Koch, B. Mapping an invasive plant Spartina alterniflora by combining an ensemble one-class classification algorithm with a phenological NDVI time-series analysis approach in middle coast of Jiangsu, China. *Remote Sens.* **2020**, *12*, 4010. [CrossRef]
46. Pix4Dmapper 2022. Available online: http://www.pix4d.com (accessed on 23 June 2022).
47. Applied Imagery QT Modeler 2021. Available online: http://www.appliedimagery.com (accessed on 1 August 2021).
48. Environmental Systems Research Institute. *ArcGIS Pro*, Version 3.0.2; Environmental Systems Research Institute: Redlands, CA, USA, 2022.
49. Isenberg, M. *LAStools—Efficient LiDAR Processing Software*, Version 221128; Academic: Cambridge, MA, USA, 2022. Available online: http://www.rapidlasso.com/LAStools(accessed on 1 August 2022).
50. GDAL/OGR Contributors. GDAL/OGR Geospatial Data Abstraction Software Library. *Open Source Geospatial Foundation.* 2022. Available online: https://gdal.org/ (accessed on 1 August 2022).
51. Baatz, M.; Schape, A. Multiresolution segmentation: An optimized approach for high quality multi-scale image segmentation. In *Angewandte Geographische Informations-Verarbeitung XII*; Wichmann: Heidelberg, Germany, 2000; pp. 12–23.
52. Blaschke, T. Object based image analysis for remote sensing. *ISPRS J. Photogramm. Remote Sens.* **2010**, *65*, 2–16. [CrossRef]
53. Benz, U.C.; Hofmann, P.; Willhauck, G.; Lingenfelder, I.; Heynen, M. Multi-resolution, object-oriented fuzzy analysis of remote sensing data for GIS-ready information. *ISPRS J. Photogramm. Remote Sens.* **2004**, *58*, 239–258. [CrossRef]
54. Han, N.; Du, H.; Zhou, G.; Xu, X.; Ge, H.; Liu, L.; Gao, G.; Sun, S. Exploring the synergistic use of multi-scale image object metrics for land-use/land-cover mapping using an object-based approach. *Int. J. Remote Sens.* **2015**, *36*, 3544–3562. [CrossRef]
55. Du, B.; Mao, D.; Wang, Z.; Qiu, Z.; Yan, H.; Feng, K.; Zhang, Z. Mapping Wetland Plant Communities Using Unmanned Aerial Vehicle Hyperspectral Imagery by Comparing Object/Pixel-Based Classifications Combining Multiple Machine-Learning Algorithms. *IEEE J. Sel. Top. Appl. Earth Obs. Remote Sens.* **2021**, *14*, 8249–8258. [CrossRef]
56. Adugna, T.; Xu, W.; Fan, J. Comparison of Random Forest and Support Vector Machine Classifiers for Regional Land Cover Mapping Using Coarse Resolution FY-3C Images. *Remote Sens.* **2022**, *14*, 574. [CrossRef]
57. Raczko, E.; Zagajewski, B. Comparison of support vector machine, random forest and neural network classifiers for tree species classification on airborne hyperspectral APEX images. *Eur. J. Remote Sens.* **2017**, *50*, 144–154. [CrossRef]
58. Thanh Noi, P.; Kappas, M. Comparison of Random Forest, k-Nearest Neighbor, and Support Vector Machine Classifiers for Land Cover Classification Using Sentinel-2 Imagery. *Sensors* **2017**, *18*, 18. [CrossRef]
59. Shiferaw, H.; Bewket, W.; Eckert, S. Performances of machine learning algorithms for mapping fractional cover of an invasive plant species in a dryland ecosystem. *Ecol. Evol.* **2019**, *9*, 2562–2574. [CrossRef]
60. Trimble Germany GmbH. *eCognition Developer*, Version 10.2; Trimble Germany GmbH: Munich, Germany, 2022.
61. Python Software Foundation. *Python Programming Language*, Version 3.7; Python Software Foundation: Wilmington, DE, USA, 2021.
62. Brooks, C.; Weinstein, C.; Poley, A.; Grimm, A.; Marion, N.; Bourgeau-Chavez, L.; Hansen, D.; Kowalski, K. Using uncrewed aerial vehicles for identifying the extent of invasive *Phragmites australis* in treatment areas enrolled in an adaptive management program. *Remote Sens.* **2021**, *13*, 1895. [CrossRef]
63. Wang, X.; Wang, M.; Wang, S.; Wu, Y. Extraction of vegetation information from visible unmanned aerial vehicle images. *Chinese Soc. Agric. Eng.* **2015**, *31*, 152–159. [CrossRef]
64. Pedregosa, F.; Varoquaux, G.; Gramfort, A.; Michel, V.; Thirion, B.; Grisel, O.; Blondel, M.; Prettenhofer, P.; Weiss, R.; Dubourg, V.; et al. Scikit-learn: Machine Learning in Python. *J. Mach. Learn. Res.* **2011**, *12*, 2825–2830.
65. Belgiu, M.; Drăgu, L. Random forest in remote sensing: A review of applications and future directions. *ISPRS J. Photogramm. Remote Sens.* **2016**, *114*, 24–31. [CrossRef]
66. Larson, K.B.; Tuor, A.R.; Larson, K.B.; Tuor, A.R.; Bazzichetto, M. Deep Learning Classification of Cheatgrass Invasion in the Western United States Using Biophysical and Remote Sensing Data Citation: Deep Learning Classification of Cheatgrass Invasion in the Western. *Remote Sens.* **2021**, *13*, 1246. [CrossRef]
67. Zhang, Y.; Liu, J.; Shen, W. A Review of Ensemble Learning Algorithms Used in Remote Sensing Applications. *Appl. Sci.* **2022**, *12*, 8654. [CrossRef]
68. Minka, T.P. Automatic choice of dimensionality for PCA. In *Advances in Neural Information Processing Systems*; NeurIPS Proceedings: New Orleans, LA, USA, 2001.
69. Kingma, D.P.; Ba, J.L. Adam: A method for stochastic optimization. In Proceedings of the 3rd International Conference on Learning Representations, ICLR 2015, San Diego, CA, USA, 7–9 May 2015; pp. 1–15.
70. Trimble Germany GmbH. *Trimble Documentation eCognition Developer 10.2 User Guide*; Trimble Germany GmbH: Munich, Germany, 2022.
71. Haralick, R.M.; Shanmugam, K.; Dinstein, I. Textural Features for Image Classification. *IEEe Trans. Syst. Man Cybern.* **1973**, *3*, 610–621. [CrossRef]
72. Congalton, R.G.; Green, K. *Assessing the Accuracy of Remotely Sensed Data: Principles and Practices*, 3rd ed.; CRC Press: Boca Raton, FL, USA, 2019.

73. Taha, A.A.; Hanbury, A. Metrics for evaluating 3D medical image segmentation: Analysis, selection, and tool. *BMC Med. Imaging* **2015**, *15*, 29. [CrossRef]
74. Chicco, D.; Jurman, G. The advantages of the Matthews correlation coefficient (MCC) over F1 score and accuracy in binary classification evaluation. *BMC Genom.* **2020**, *21*, 6. [CrossRef] [PubMed]
75. Guo, Y.; Zhao, Y.; Rothfus, T.A.; Avalos, A.S. A novel invasive plant detection approach using time series images from unmanned aerial systems based on convolutional and recurrent neural networks. *Neural Comput. Appl.* **2022**, *34*, 20135–20147. [CrossRef]
76. Husson, E.; Ecke, F.; Reese, H. Comparison of manual mapping and automated object-based image analysis of non-submerged aquatic vegetation from very-high-resolution UAS images. *Remote Sens.* **2016**, *8*, 724. [CrossRef]
77. Pricope, N.G.; Mapes, K.L.; Woodward, K.D.; Olsen, S.F.; Baxley, J.B. Multi-Sensor Assessment of the Effects of Varying Processing Parameters on UAS Product Accuracy and Quality. *Drones* **2019**, *3*, 63. [CrossRef]
78. Clapuyt, F.; Vanacker, V.; Van Oost, K. Reproducibility of UAV-based earth topography reconstructions based on Structure-from-Motion algorithms. *Geomorphology* **2016**, *260*, 4–15. [CrossRef]

Disclaimer/Publisher's Note: The statements, opinions and data contained in all publications are solely those of the individual author(s) and contributor(s) and not of MDPI and/or the editor(s). MDPI and/or the editor(s) disclaim responsibility for any injury to people or property resulting from any ideas, methods, instructions or products referred to in the content.